THE EFFECT OF R-RATIO ON THE MODE II FATIGUE DELAMINATION GROWTH OF UNIDIRECTIONAL CARBON/EPOXY COMPOSITES

by

Livio R. Gambone

B.Eng., McGill University, 1987

A THESIS SUBMITTED IN PARTIAL FULFILLMENT OF

THE REQUIREMENTS FOR THE DEGREE OF

MASTER OF APPLIED SCIENCE

in

THE FACULTY OF GRADUATE STUDIES

Department of Metals and Materials Engineering

We accept this thesis as conforming

to the required standard

THE UNIVERSITY OF BRITISH COLUMBIA

April 1991

In presenting this thesis in partial fulfilment of the requirements for an advanced degree at the University of British Columbia, I agree that the Library shall make it freely available for reference and study. I further agree that permission for extensive copying of this thesis for scholarly purposes may be granted by the head of my department or by his or her representatives. It is understood that copying or publication of this thesis for financial gain shall not be allowed without my written permission.

Department of Metals and Materials Engineering

The University of British Columbia
Vancouver, Canada

Date April 30, 1991

DE-6 (2/88)

ABSTRACT

An investigation of the effect of R-ratio on the mode II fatigue delamination of AS4/3501-6 carbon/epoxy composites has been undertaken. Experiments have been performed on end notched cantilever beam specimens over a wide range of R-ratios ($-1 \leq R \leq 0.50$). The measured delamination growth rate data have been correlated with the mode II values of strain energy release rate range (ΔG_{II}), maximum strain energy release rate (G_{IImax}) and stress intensity factor range (ΔK_{II}). The growth rate is dependent on the R-ratio over the range tested. For a constant level of ΔG_{II}, the crack growth rate decreases with increasing R-ratio. A similar trend is observed when the data is plotted as a function of G_{IImax}. The effect of plotting the growth rate as a function of ΔK_{II} is to produce an R-ratio dependence opposite to that obtained by either the ΔG_{II} or G_{IImax} approach. For a constant level of ΔK_{II}, the crack growth rate increases with increasing R-ratio.

Master equations which completely characterize the fatigue behaviour as a function of ΔG_{II} and ΔK_{II} have been derived, based on the observation that the growth rate law exponent, n and constant, A are unique functions of R-ratio. Values for n are surprisingly large and increase with increasing R-ratio whereas values for A decrease with increasing R-ratio.

The effect of time-at-load has been considered in an attempt to explain the existence of the R-ratio dependence of the growth rate. The correct trend can be established for the exponent, n but not for the constant, A. Friction between the crack faces, particularly at higher R-ratios, is proposed as a possible explanation for the observed anomaly. Further evidence of a frictional mechanism operating at higher R-ratios has been discovered through a postmortem fracture surface examination.

Additional fractographic observations are presented over the entire range of R-ratios tested. In regions subjected to negative R-ratio cycling, there is no evidence of the characteristic

mode II hackle features. Instead, loose rounded particles of matrix material are found. An extensive amount of hackling is observed in regions subjected to low positive R-ratio cycles. The extent of hackle damage visibly decreases in areas where higher levels of R-ratio are imposed. A correlation between the general fracture surface morphology and the fatigue data provides support for the hypothesis that energy for delamination is always available in sufficient quantity, and that growth is dependent on the stresses ahead of the crack tip being sufficiently high.

TABLE OF CONTENTS

LIST OF FIGURES

LIST OF TABLES

NOMENCLATURE

a	delamination crack length (m)
a_{ij}	orthotropic material elastic constants (1/Pa)
A	fatigue growth rate law constant
$A_{G,K}$	fatigue growth rate law constant pertaining to strain energy release rate and stress intensity analyses respectively
$A_{apparent}$	fatigue growth rate law constant for combined "true" fatigue plus time-at-load effects
A_{-1}	fatigue growth rate law constant for R = -1 loading case
b	specimen width (m)
B	static growth rate law constant for time at load case
C	specimen compliance (m/N)
C_o	compliance due to specimen transverse shear and end gripping fixture (m/N)
DCB	double cantilever beam
E	flexural modulus for isotropic material (GPa)
E'	flexural modulus for mode I orthotropic case (GPa)
E''	flexural modulus for mode II orthotropic case (GPa)
ENCB	end notched cantilever beam
f	frequency (Hz)
f_{ij}	stress intensity function
F	work performed by external force on cracked body (J/m)
G	strain energy release rate (J/m^2)
G_{th}	no-delamination growth threshold value of strain energy release rate (J/m^2)
G_{II}	mode II component of strain energy release rate (J/m^2)
$G_{IImin,max}$	minimum and maximum value of strain energy release rate in a cycle (J/m_2)
G_{IIth}	mode II component of no-delamination growth threshold value of strain energy release rate (J/m^2)

ΔG	strain energy release rate range (J/m^2)
ΔG_{II}	mode II component of strain energy release rate range (J/m^2)
h	specimen half thickness (m)
K	stress intensity factor ($MPa\sqrt{m}$)
K_c	critical value of stress intensity factor ($MPa\sqrt{m}$)
$K_{min,max}$	minimum and maximum value of stress intensity factor in a cycle ($MPa\sqrt{m}$)
K_{mean}	average value of stress intensity factor in a cycle ($MPa\sqrt{m}$)
K_{II}	mode II component of stress intensity factor ($MPa\sqrt{m}$)
$K_{IImin,max}$	minimum and maximum value of mode II component of stress intensity factor in a cycle ($MPa\sqrt{m}$)
ΔK	stress intensity factor range ($MPa\sqrt{m}$)
ΔK_{th}	threshold value of stress intensity factor range ($MPa\sqrt{m}$)
ΔK_{II}	mode II component of stress intensity factor range ($MPa\sqrt{m}$)
L	specimen length (m)
LEFM	linear elastic fracture mechanics
LVDT	linear variable displacement transducer
m	static growth rate law exponent for time-at-load case
MMF	mixed mode flexure
n	fatigue growth rate law exponent
$n_{G,K}$	fatigue growth rate law exponent pertaining to strain energy release rate and stress intensity analyses respectively
$n_{apparent}$	fatigue growth rate law exponent for combined "true" fatigue and time-at-load effects
n_{-1}	fatigue growth rate law exponent for R = -1 loading case
N	number of cycles
P	applied load (N)

r	radial distance from crack tip (m)
R	stress ratio
R_c	crack growth resistance (J/m^2)
t	time (sec)
U	elastic energy stored in cracked body (J/m)
W	energy available for crack growth in a cracked body (J/m)
δ	applied deflection (m)
$\delta_{min,max}$	minimum and maximum value of applied deflection in a cycle (m)
θ	angle to crack plane
σ_{ij}	local stress field for crack in infinite body (Pa)
$\sigma_{min,max}$	minimum and maximum value of stress in a cycle (Pa)

ACKNOWLEDGEMENT

I am greatly indebted to Professor A. Poursartip for his guidance, advice and technical assistance throughout the course of this study. His enthusiasm in the pursuit of answers has taught me to always question. I wish to thank Mr. A.J. Russell and Dr. K.N. Street of the Defense Research Establishment Pacific who contributed greatly through their insightful discussions and by furnishing the test coupons. I am also grateful to the Natural Sciences and Engineering Research Council of Canada for providing funding for this work in the form of a postgraduate scholarship. Finally, special gratitude is due to those individuals who over a period of several years offered their suggestions and warm encouragement: Mr. N.S. Chinatambi, Mr. R.Bennett, Mr. G. Smith, Capt. S. Ferguson and Ms. M. Hilborn.

1 INTRODUCTION

1.1 Background

A considerable amount of attention has been focused on fibre reinforced composites as the need for stronger and lighter structures has become more prevalent over the last several decades. In fact, the attractiveness of laminated composites led to their use as structural materials in the aerospace industry from as early as 1953 when the Martin Marietta Corporation began manufacturing filament wound glass/epoxy rocket motor casings. In 1968, the McDonnell Douglas Corporation experimented with the use of boron/epoxy rudders on some of the last production models of the F-4 Phantom. These successes in conjunction with the emergence of carbon/epoxy technology led to increased confidence in the use of composite systems in regular production fighter aircraft such as the F-15 Eagle, F-18 Hornet and AV-8B Harrier, and commercial aircraft such as the Boeing 727, 737, 757 and 767.

The most influential feature governing the choice of material and form of construction for any aircraft component part is its structural integrity classification. This falls into three categories: *primary structures* whose failure would seriously endanger the aircraft (typical components are wing, tail unit and main flaps); *secondary structures* whose failure, while not being catastrophic, would permit continued flight, but with a seriously restricted flight capability (these components are represented by control surfaces such as ailerons, rudder and some engine nacelle components); and *non-critical structures* whose failure have no safety implications and only minor effects on flight performance and handling characteristics (streamline fairing structures and small access doors are examples of these types of components which are generally subject to low loadings by definition) [1].

Currently, composite materials are no longer solely reserved for use as the occasional panel blended in to reduce weight. A broad range of materials and structures are used in applications extending from non-critical fairings to components which require the integrity of primary structures. Horizontal and vertical stabilizers, wing skins, spars, ribs and a variety of avionics panels and doors represent the new structural applications for composites [1].

Airbus Industrie makes extensive use of composites in the tail section of the A320 commercial airliner where both the horizontal and vertical stabilizers are mainly carbon/epoxy. Research at Airbus is currently being conducted on metal fuselage replacement feasibility. An aluminum alloy fuselage lasts about two minutes in a post crash fuel fire, after which collapse and melting may occur. The Federal Aviation Association would like to see fuselages last five minutes. Airbus has evidence from panel tests that a composite sandwich fuselage could last 50 minutes [2].

An interesting advantage of aerospace structures made from composites is the iterative weight saving capability these materials possess. If a structural weight of one ton is saved through the use of composites, then the take-off weight of the aircraft is reduced by 1.52 tons due to reduced fuel consumption. This allows for a redesign of the structure saving another 0.12 tons which feeds back into the system giving a final reduction in take-off weight of 1.74 tons. This effect is quite significant when the associated monetary savings is also considered. A weight reduction of 1 kg translates to a savings of about $1000 (U.S.) over the life of the aircraft, depending on the use and cost of the part [2].

1.2 Motivation

The increasing use of laminated composites in primary and secondary structural components in modern aircraft has necessitated the characterization of the failure mechanisms

of these materials. One of the most frequently encountered defects in exposed composite aircraft structures is delamination. Delamination is the inability to resist defect initiation and subsequent crack growth in the interlaminar plane, i.e. between the layers of the composite laminate. The characterization of delamination is therefore fundamental to the evaluation of composites for durability and damage tolerance.

A large number of tests have been conducted over the years in order to establish a framework for damage tolerant design for isotropic materials such as metals and polymers. Close to $1 billion (U.S.) a year is currently being spent worldwide on fatigue testing alone to provide the data base for metal fatigue design [3]. Unlike metals, composite laminates possess the capability of being fabricated into many different stacking configurations. At the design stage, only a limited amount of testing is possible due to the cost. This decreases the likelihood of the establishment of a comprehensive data base on the fatigue behaviour. For this reason, researchers are interested in developing a formulation for predicting the full scale structural damage tolerance based on coupon testing and analytical considerations [4]. The objective is to develop a cumulative damage model for predicting the evolution of damage growth in composite laminates subjected to a mechanical loading scheme representative of that found in service.

The data base approach however, is nevertheless an important aspect in the characterization of the delamination of composites as attested by the large attention it has been given in recent years (e.g. [5]). The generation of a data base is linked to the development of a fracture mechanics methodology which may assess defect criticality and predict fatigue crack growth rates, so that appropriate repairs can be made in a timely manner [6].

The purpose of the current investigation therefore, is to both generate new fatigue data on carbon/epoxy composites through the examination of the effect of R-ratio on the shear loading of delaminated unidirectional specimens, and attempt to explain the results in a framework that will allow the development of a damage tolerant methodology.

The response of the composite system to the R-ratio variable (a ratio of the minimum to maximum stress in a fatigue cycle) will provide valuable insight into the failure mechanisms involved. As a result, a sound data base coupled with a mechanistic understanding of fatigue failure might evolve.

2 APPROACH

2.1 Basics

Consider the schematic of a typical composite laminate shown in Figure 2.1. Layers of unidirectional fibres in a resin matrix are stacked at various orientations relative to one another and cured under heat and pressure. The laminate strength is determined by the particular order and orientation of fibres in the principal material directions. Optimization of the laminate strength, stiffness, weight and/or thermal expansion is possible once the applied stresses are known.

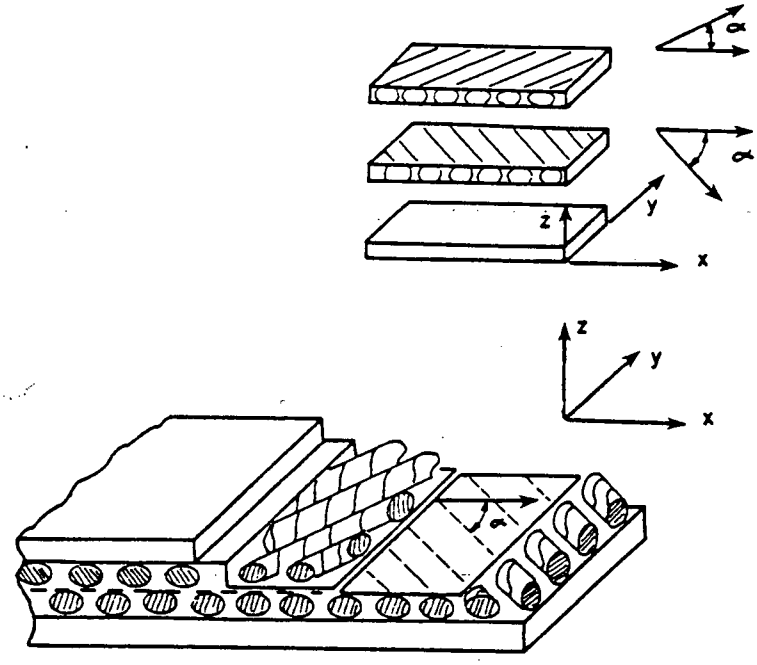

Figure 2.1 Schematic representation of typical composite laminate [7].

The in-plane strengths of the laminate shown in Figure 2.1 is therefore a function of the orientation of the fibres in the x-y plane. The strength in the z-direction is determined primarily by the strength of the weaker matrix material. Laminates are typically not designed to support

out-of-plane loads, but this is often unavoidable due to design constraints. Load path discontinuities such as those shown in Figure 2.2 result in significant stresses in the z-direction. These interlaminar normal and shear stresses inevitably lead to delamination. A delamination is not necessarily a serious failure under tensile loading as there are often redundant load paths through the laminate. A delamination subjected to compressive stresses however, results in a decrease in the laminate thickness and a significant reduction in the critical buckling load of the component.

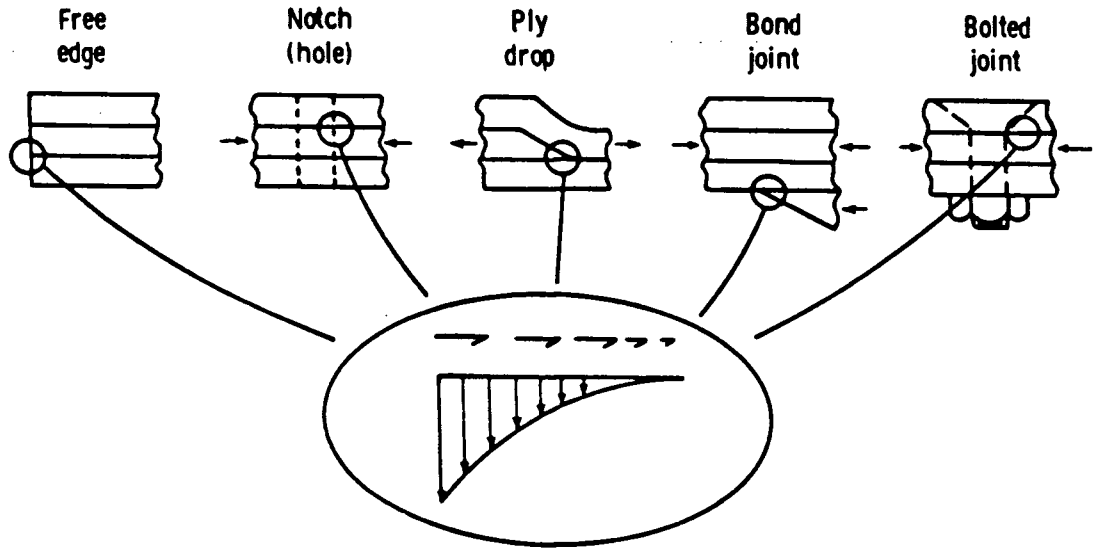

Figure 2.2 Sources of out-of-plane loads from load path discontinuities [8].

To simplify the analysis of the resistance of a composite structure to delamination, the stresses at the delamination or crack tip are viewed as a superposition of three pure mode loadings as shown in Figure 2.3. Mode I, which is known as the opening mode, results when the surface of the delamination is displaced normal to the defect plane. Mode II is known as the sliding

shear mode and is characterized by crack surface displacements in the plane of the crack and normal to the crack front. Finally, Mode III or tearing shear mode results when the crack surfaces are displaced in the plane of the crack and parallel to the crack front.

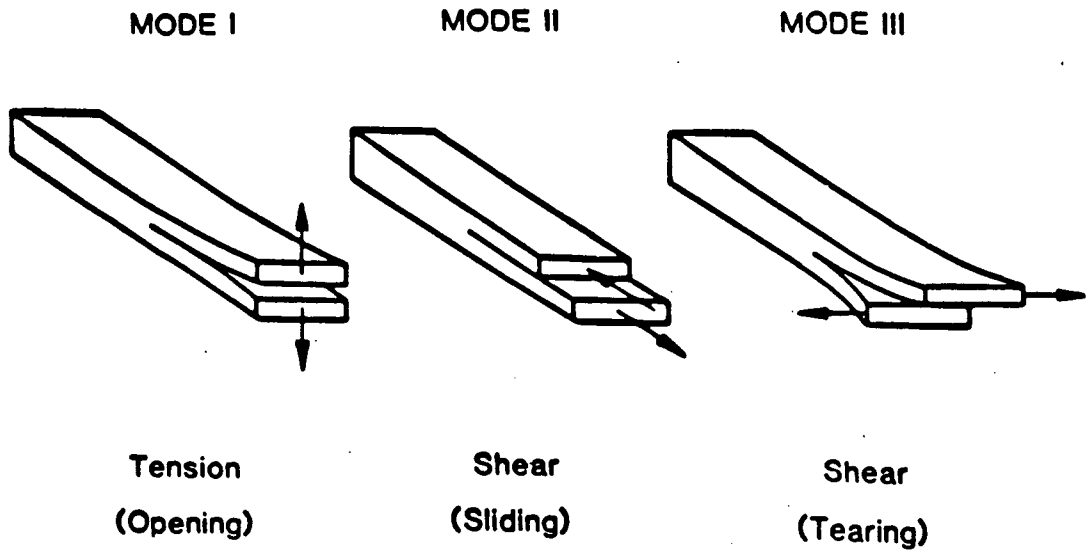

Figure 2.3 Delamination fracture modes [8].

2.2 Linear Elastic Fracture Mechanics

Linear elastic fracture mechanics (LEFM) is used extensively in the failure prediction of metallic structures. When a crack in a plate reaches a certain size the stress intensity factor K, which is a function of the load, loading geometry and crack size, exceeds the fracture toughness, K_c and failure occurs as the crack propagates, separating the plate into two pieces.

The principle of an elastic stress field in a cracked body is well documented in the literature (e.g.[9,10]). Based on the orientation shown in Figure 2.4, the local stress field for a crack of length $2a$ in an infinite body may be expressed as

$$\sigma_{ij} = \frac{K}{\sqrt{2\pi r}} f_{ij}(\theta) \tag{2.1}$$

where K is the stress intensity factor and is equal to $\sigma\sqrt{\pi a}$ for a centre-cracked infinite panel, r is the radial distance from the crack tip and $f_{ij}(\theta)$ represents a function which describes the dependence of the stress magnitude, σ on the θ direction. It is evident from equation (2.1) that the local stresses tend to infinity approaching the crack tip. This singular stress state does not occur in reality as plasticity at the crack tip keeps the stress level finite.

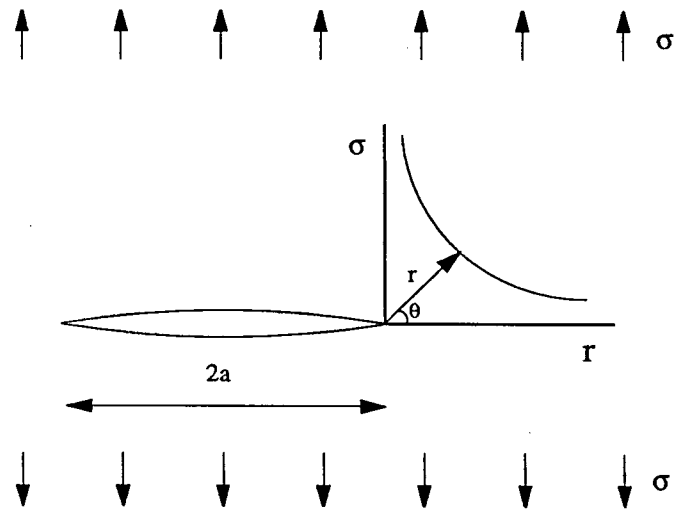

Figure 2.4 Crack tip stress field in an infinite plate.

The difference between two cracked components is represented by a change in the magnitude of K, which is a function of the configuration of the cracked components and the type of applied loads. Stress intensity solutions exist for many different crack geometries (e.g. [11]).

The applicability of LEFM to the fracture and failure of composite materials has been an issue of great importance and controversy over the past two decades. It is not clear whether LEFM is applicable to the in-plane tensile loading of composite materials [12-14]. Evidently, the experimental characterization of the in-plane fracture toughness of composites can be quite complicated because self-similar crack growth, which occurs in homogeneous isotropic materials, usually does not occur in composite materials. In addition, fracture toughness tests cannot be interpreted easily resulting in time consuming analysis. For example, the approach described in Ref [12] approximated a flaw using a center crack in a 90° unidirectional plate under tension. Unstable crack growth resulted, leading to catastrophic failure producing only one data point.

However, considerable data exists on the application of LEFM to delamination growth in composite laminates. Contemporary interlaminar fracture tests typically use a thick (24 ply or more) unidirectional composite specimen with a Teflon insert at the midplane as a starter crack. The crack is grown by subjecting the specimen to a bending load to induce shear or by wedging the crack open to induce tension. The results are interpreted using the strain energy release rate approach, as described in the next section. In general, the data reduction is much simpler than for in-plane fracture testing. Several examples of these tests include the double cantilever beam (DCB) test (mode I), the end notched flexure (ENF) test (mode II), the end notched cantilever beam (ENCB) test (mode II) and the mixed mode flexure (MMF) test (mixed modes I/II).

2.3 Energy Method

The LEFM approach for characterizing delamination growth in composite materials is based on the strain energy release rate, G rather than the stress intensity factor, K. This is due to problems with anisotropic theory which predicts that the stress intensity singularity at the crack tip is in general a function of the orientation and moduli of the adjacent composite layers and is not only of a simple $r^{-1/2}$ form as shown in equation (2.1). In fact, equation (2.1) possesses an oscillatory component for many lay-ups [15]. This is physically impossible as it implies that the crack faces interpenetrate. On the other hand, the strain energy release rate is mathematically well defined and is easily related to measurable quantities.

The Griffith energy criterion for fracture [16] can be interpreted to mean that crack growth can occur if the energy required to form an additional crack of size da can just be delivered by the system. The energy balance corresponding to this statement for a plate of unit thickness may be expressed as

$$\frac{d(F-U)}{da}=\frac{dW}{da} \tag{2.2}$$

where F is the work performed by the external force, U is the elastic energy stored in the body and W is the energy for crack formation. The strain energy release rate or crack driving force, G and the crack resistance, R_c are defined as

$$G=\frac{d(F-U)}{da} \tag{2.3}$$

$$R_c=\frac{dW}{da} \tag{2.4}$$

Consider a cracked plate of thickness b subjected to a load P as shown in Figure 2.5. The elastic energy contained in the cracked plate is

$$U = \frac{1}{2} P\delta = \frac{1}{2} CP^2 \tag{2.5}$$

where P is the applied load, δ is the resulting displacement and C is the compliance ($C = \delta/P$). When the crack increases in length by da, the work done by the external force is

$$F = P\,d\delta = P\,d(CP) \tag{2.6}$$

The strain energy release rate can therefore be written as

$$G = \frac{1}{b}\left(P\frac{d(CP)}{da} - \frac{1}{2}\frac{d(CP^2)}{da} \right) \tag{2.7}$$

which may be differentiated to yield

$$G = \frac{P^2}{2b}\left(\frac{\partial C}{\partial a} \right) \tag{2.8}$$

It is important to note that the strain energy release rate is independent of whether or not the load is constant and is always equal to the derivative of the elastic energy for small crack lengths, i.e. da. Mathematically, this may be expressed as

$$G = \frac{1}{b}\left(\frac{dU}{da} \right)_P = -\frac{1}{b}\left(\frac{dU}{da} \right)_\delta \tag{2.9}$$

At constant load U increases and at constant displacement U decreases.

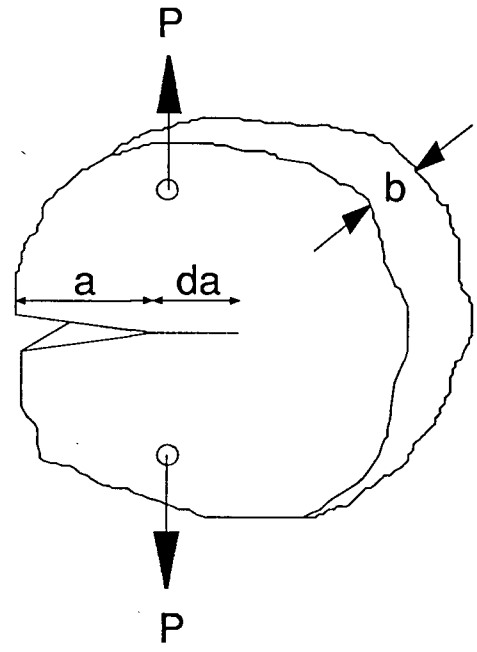

Figure 2.5 Elastic plate containing a crack.

The strain energy release rate may also be derived graphically. Consider the load-displacement diagram represented in Figure 2.6. When the load is fixed and crack extension occurs, the displacement increases and the strain energy release rate may be visualized as the area of triangle OAE. When crack extension occurs under fixed displacement, the load drops and the strain energy release rate is represented by the area of triangle OAB. For infinitely small *da*, the small triangle AEB can be neglected and areas OAE and OAB are equivalent. Thus the energy available for crack growth is the same in both cases.

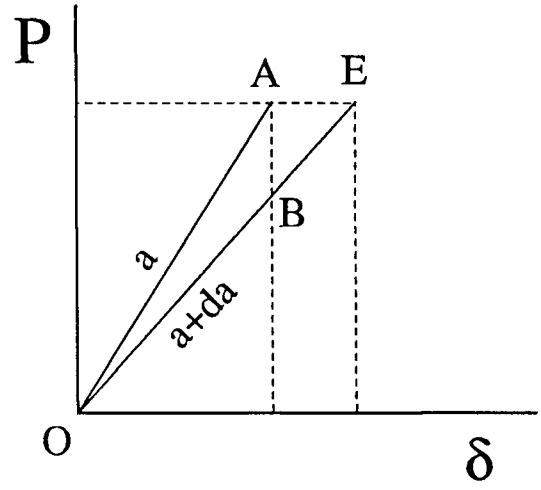

Figure 2.6 Load-displacement diagram.

2.4 Fatigue

The performance of composite materials is typically assessed by considering parameters such as the stiffness, strength and fatigue life. Stiffness is predicted by a mechanics of solids approach or through the extension of Hooke's Laws for isotropic materials via laminated plate theory. Strength is predicted with the application of a failure criterion such as the Tsai-Hill criteria [17]. This theory was derived by Tsai [18] from a yield criterion for anisotropic materials originally proposed by Hill [19]. Under cyclic loading conditions, composite fatigue life is based on the reduction of stiffness and strength over time due to delamination, matrix cracking and fibre breakage. Of these damage mechanisms, delamination growth is considered to be the most detrimental [6]. Since a delamination can be regarded as a crack, the application of an LEFM methodology to fatigue life prediction makes sense.

It has been proposed [20] that for delamination growth in composites, fatigue life be separated into initiation and growth. Based on the assumption that all materials contain initial flaws in the form of material discontinuities or manufacturing defects such as voids, inclusions or broken fibres, it follows that in service these flaws initiate as delaminations or matrix cracks. Upon initiation, a delamination will grow and obey some growth law. Since LEFM applies, life prediction may be based on a slight modification of the Paris Law [21]

$$\frac{da}{dN} = A(\Delta K)^n \tag{2.10}$$

where ΔK may be replaced by the cyclic strain energy release rate range, ΔG [22].

The characterization of mode I fatigue delamination has received considerable attention in the literature [e.g.6,22-24]. These studies have shown that correlations between measured delamination growth rates and the corresponding strain energy release rates result in a power law relationship of the form of equation (2.10). Similar results have been reported for mode II cyclic loading [e.g.6,25,26].

Attention has recently been focused on the effect of R-ratio on composite fatigue delamination [6,25,27-31]. The R-ratio is defined as the ratio of the minimum to maximum stress of the fatigue cycle (see equation (2.13)). For metals, equation (2.10) does not fully represent reality as actual data tends to fall on an S-shaped curve such as the one shown schematically in Figure 2.7. When the R-ratio is non-zero, the stress intensity range, ΔK is no longer sufficient in describing the stress state at the crack tip over the entire range of ΔK. In fact, the power law relationship for fatigue crack growth in metals is usually characterized by specifying any two of the following parameters: K_{max}, K_{min}, K_{mean}, ΔK, R where

$$\Delta K = K_{\max} - K_{\min} \tag{2.11}$$

$$K_{mean} = \frac{K_{min} + K_{max}}{2} \tag{2.12}$$

$$R = \frac{\sigma_{min}}{\sigma_{max}} = \frac{K_{min}}{K_{max}} \tag{2.13}$$

The following is therefore true,

$$\frac{da}{dN} = f_1(\Delta K, K_{max}) = f_2(\Delta K, R) = f_3(K_{max}, R) \tag{2.14}$$

The relationship described in equation (2.14) is particularly significant at low and high ΔK as shown in Figure 2.7. At low ΔK (region 1), crack propagation is slow and approaches a threshold value below which there is no measureable growth. At high ΔK (region 3), the crack growth rate tends to infinity as the crack length approaches the critical size, i.e. when K_{max} equals K_c. Attempts have been made to modify equation (2.10) to reflect these trends, but the majority are only reasonably satisfactory in a limited region for limited sets of data. This is a reflection of the fact that any modification is in essence an empirical modification. The most notable of these is the Forman equation [32]

$$\frac{da}{dN} = \frac{A(\Delta K)^n}{(1-R)(K_c - K_{max})} \tag{2.15}$$

For metals, at ΔK levels near the threshold region (region 1 in Figure 2.7), crack closure causes an R-ratio dependence of the growth rate. Crack closure occurs when the elastic surroundings exert compressive stresses on the plastically deformed material at the crack tip [9]. Although the effect of crack closure on unidirectional carbon/epoxy composites is negligible, there still exists evidence of a dependence of growth rate on R-ratio in the power

law region (region 2 in Figure 2.7).

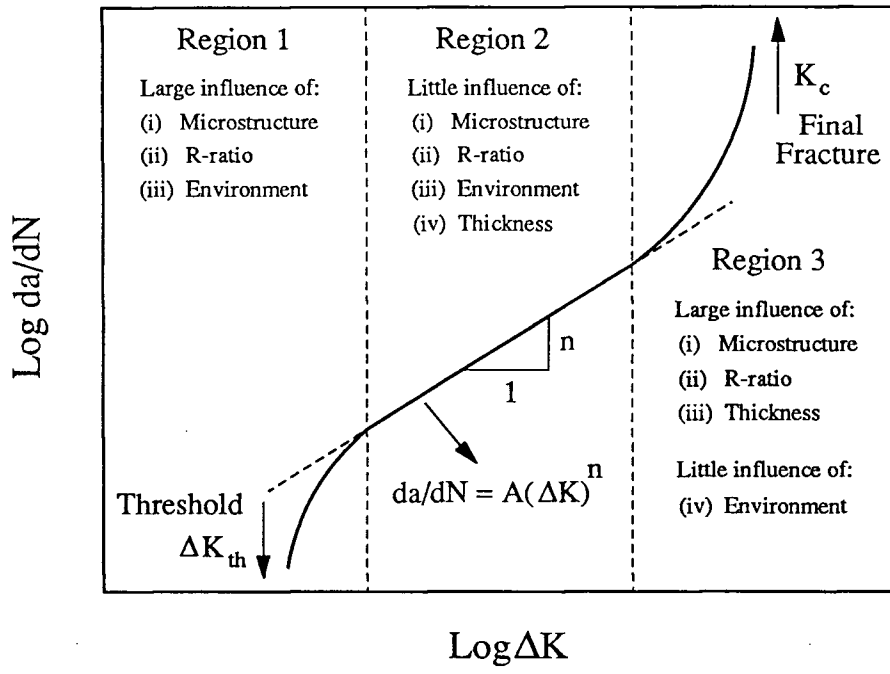

Figure 2.7 Schematic variation of fatigue crack growth rate with stress intensity range in steels [33].

Previous studies [27,28] on several different carbon composite systems (AS4/PEEK, T300/914C, T300/P305) tested in mode I showed that at a constant level of ΔK, the crack growth rate increased with increasing R-ratio. Plotting the crack growth rate data as a function of ΔG however, showed no effect of R-ratio for T300/914C specimens, whereas the crack growth rate decreased with increasing R-ratio at a constant ΔG for T300/P305 specimens [28]. These differences were attributed to the nature of the two resins resulting in dissimilar fatigue crack propagation mechanisms as observed in a postmortem analysis. The fracture surface features

on the specimens that showed no effect of R-ratio on growth rate as a function of ΔG indicated the existence of a purely matrix fracture dominated failure mechanism. In instances where R-ratio affected the growth rate, a fibre/matrix interfacial debonding mechanism was observed.

Mode I tests carried out on an AS4/PEEK carbon composite system also showed a decrease in crack growth rate with increasing R-ratio but at a constant level of maximum strain energy release rate, G_{max} [29]. The reasoning for this observation was based on the difference in magnitude of ΔG at different R-ratios. By definition, at low values of R-ratio, ΔG is higher in magnitude than at high values of R-ratio even though G_{max} is the same. These results hinted that perhaps ΔG alone was the controlling variable for fatigue crack growth.

Interestingly, evidence from the mode I testing of adhesively bonded T300/5208 carbon/epoxy composite joints suggested the same trend [30]. Plotting the growth rate as a function of G_{max} revealed that increasing R-ratio led to a decrease in growth rate. The same data plotted as a function of ΔG however, fell along a single straight line within a scatter band, independent of R-ratio. These results were not surprising in light of the postmortem observations made for the T300/914C specimens in Ref [28]. The similarity between crack growth through an adhesive layer in Ref [30] and matrix fracture in Ref [28] was striking. Not surprisingly, identical conclusions were inevitable, i.e. that ΔG alone was the driving parameter for cyclic debonding.

Although there exists a relatively scarce amount of published data concerned with the effect of R-ratio on delamination growth rate in modes II and III, there is at least consistency in the findings. Work carried out on numerous carbon composite systems (AS1/3501-6, AS4/2220-3, C6000/F155, AS4/PEEK) indicated that at a constant level of ΔG, the crack growth rate decreased when the R-ratio was increased from R = -1 to R = 0 [6,25]. Postmortem fractography revealed that the micromechanical damage mechanisms controlling crack

extension were more degrading under conditions of fully reversed shear (R = -1) than at R = 0. An increase in R-ratio resulted in a similar decrease in crack growth rate but at a constant level of G_{max} for AS4/PEEK specimens tested in mode II [29]. Finally, data generated from the mode III testing of AS4/3502 carbon/epoxy specimens agreed with all the mode II findings, i.e. the crack growth rate decreased with an increase in R-ratio at constant levels of ΔG and G_{max}.

For convenience, the above results are presented in Table 2.1 in a format relevant to the current study. Only the trends generated from the data in each reference are listed. Due to the existence of a family of curves in many instances, the trend is reported as the net effect of increasing R-ratio on growth rate at a constant level of the independent variable ΔG, G_{max} and/or ΔK.

Table 2.1 Effect of increasing R-ratio on growth rate, da/dN

Fracture Mode	Material	At Constant ΔG	At Constant G_{max}	At Constant ΔK	Reference
I	AS4/PEEK	-	-	Increase	[27]
I	T300/914C	No effect	-	Increase	[28]
I	T300/P305	Decrease	-	Increase	[28]
I	AS4/PEEK	-	Decrease	-	[29]
I	T300/5208	No effect	Decrease	-	[30]
II	AS/3501	Decrease	-	-	[6]
II	AS1/3501	Decrease	-	-	[25]
II	AS4/2220	Decrease	-	-	[25]
II	C6000/F155	Decrease	-	-	[25]
II	AS4/PEEK	Decrease	-	-	[25]
II	AS4/PEEK	-	Decrease	-	[29]
III	AS4/3502	Decrease	Decrease	-	[31]

3 MODE II DELAMINATION TESTING

3.1 Fracture Specimen

An end notched cantilever beam (ENCB) specimen was chosen for mode II delamination testing due to its simple geometry and ability to grow long stable cracks. Figure 3.1 shows a schematic of the specimen geometry. The application of an end load results in flexure of the sample, thereby producing a sliding shear deformation at the crack tip.

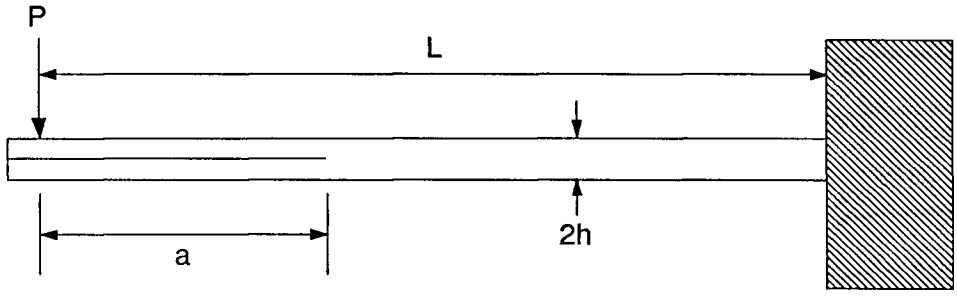

Figure 3.1 ENCB specimen geometry.

The ENCB specimens tested were fabricated at the Defense Research Establishment Pacific (DREP) from Hercules AS4/3501-6 graphite/epoxy according to the prepreg manufacturer's recommended procedures. A 0.025 mm thick folded Teflon film 35 mm in length was inserted between the plies at the midplane of each specimen to act as a delamination starter notch. The 24 layer unidirectional samples were nominally 3.3 mm thick ($2h$), 20 mm wide (b) and 110 mm long (L).

3.2 Beam Theory

The relationship between ENCB specimen compliance and delamination length has been derived previously from beam theory [17] and is represented by the expression

$$C = C_o + \frac{L^3 + 3a^3}{2Ebh^3} \tag{3.1}$$

where C is the compliance, L is the span length, a is the crack length, E is the flexural modulus, b is the width and h is the half-thickness of the sample. The constant C_o includes the specimen transverse shear compliance as well as the compliance due to the end gripping fixture.

Differentiation of equation (3.1) with respect to crack length and substitution into equation (2.8) yields the mode II strain energy release rate for the constant loading case,

$$G_{II} = \frac{9a^2P^2}{4Eb^2h^3} \tag{3.2}$$

where P is the applied load. Note that since the transverse shear compliance is independent of crack length, it has no effect on the strain energy release rate.

For the condition of constant deflection, the mode II strain energy release rate may be derived after differentiation of equation (3.1) with respect to crack length and substitution of the result as well as the definition of $P = \delta/C$ into equation (2.8) to obtain

$$G_{II} = \frac{9a^2\delta^2\left(1 - \frac{C_o}{C}\right)}{2b(L^3 + 3a^3)C} \tag{3.3}$$

where δ is the applied deflection.

3.3 Crack Growth Stability

Crack growth stability is an important consideration in the fracture testing of composite materials. The stability argument is based on the assumption that the critical strain energy release rate, G_c is a true material constant. The criterion states that crack growth must proceed in a stable manner when the rate of increase in strain energy release rate with respect to crack length is zero or negative, which is expressed mathematically as

$$\frac{\partial G}{\partial a} \leq 0 \tag{3.4}$$

For the case of mode II testing under load control, differentiation of equation (3.2) with respect to crack length yields

$$\frac{\partial G_{II}}{\partial a} = \frac{18aP^2}{4Eb^2h^3} \tag{3.5}$$

which is always a positive quantity, hence crack growth is unstable.

For the displacement control case, stability is predicted for crack length-to-span ratios greater than 0.55. This result is derived by differentiating equation (3.3) and solving for crack length, a as a function of span length, L from the resulting expression, i.e.

$$\frac{\partial G_{II}}{\partial a} = \frac{9a\delta^2}{2Eb^2h^3C^2}\left(1 - \frac{9a^3}{L^3 + 3a^3}\right) \tag{3.6}$$

where the term C_o in equation (3.3) is neglected for simplicity. The stability criterion for this case may also be determined graphically. Figure 3.2 shows a plot of G_{II} versus crack length-to-span ratio for a family of deflections applied to an ENCB specimen sized exactly as

outlined in Section 3.1. At crack length-to-span ratios less than 0.55, the strain energy available for crack extension increases, resulting in unstable crack growth. The strain energy release rate decreases at crack length-to-span ratios greater than 0.55 and thus crack growth is stable. The fixed deflection condition is experimentally advantageous as it allows for the testing of a large range of crack lengths for each specimen. For this reason, deflection control is employed in the current investigation.

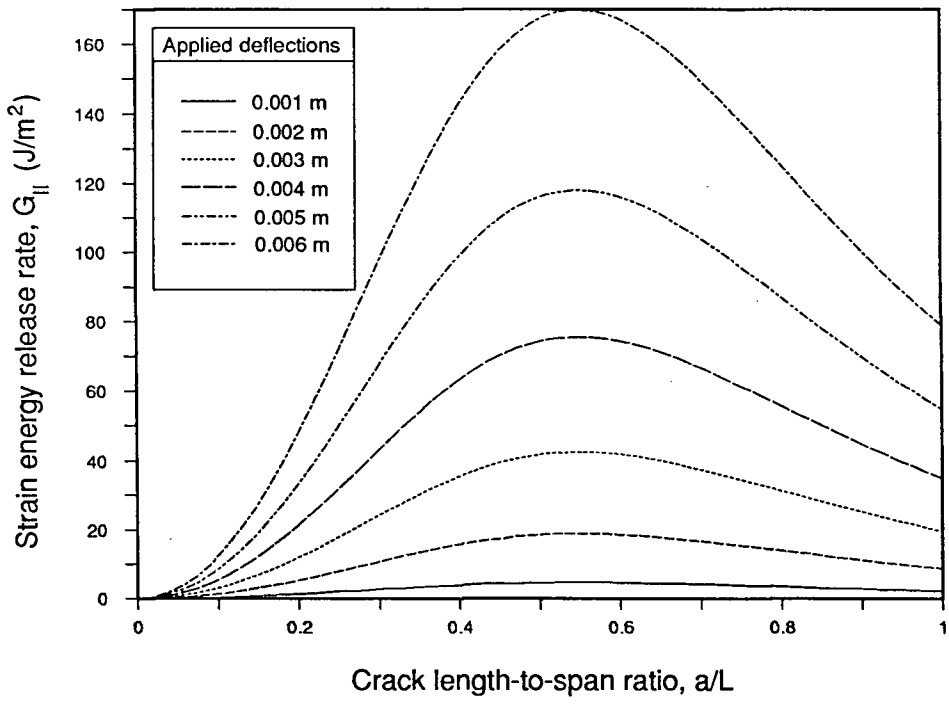

Figure 3.2 Graphical presentation of stability analysis.

4 EXPERIMENTAL PROCEDURE

4.1 Fatigue Test Setup

Figures 4.1 and 4.2 show the test fixture used in the current work. An aluminum fatigue jig with a built-in clamp was used to hold the ENCB specimen firmly at one end. A clamped roller assembly served as the load line application mechanism at the delaminated end. In order to minimize the effect of excessively high clamp pressure between the brass rollers, lock nuts that could be adjusted finger tight were used. Artificially high resistance to crack growth due to friction between the crack faces was therefore kept to a minimum for each specimen. In addition, the brass rollers were pivoted on bearings through their midsection so that free side to side rotation of the delaminated end of the specimen could occur. This reduced the variation in crack length through the specimen width.

All samples were tested in an MTS servohydraulic fatigue machine under deflection control. Loads were measured with a 4448 N (1000 lb) load cell with electronic amplification set to ×10 (so that full scale was 100 lbs), while deflections were measured with a linear variable displacement transducer (LVDT). The operation of these devices is described in Ref [34].

The MTS fatigue machine was controlled with an IBM PC microcomputer. A 12 bit resolution Qua Technologies WSB-10C digital-to-analog (D/A) waveform synthesizer board was used to generate a sine wave to control the deflection at the desired frequency and number of cycles. The load and displacement data was captured with a 12 bit resolution Data Translation DT2801-A analog-to-digital (A/D) data acquisition board. Both boards were controlled in real time with special drivers written for the Lotus Symphony spreadsheet program.

Delamination crack lengths were monitored on the back edge of the specimen with an optical travelling microscope. Each specimen was polished to a metallographic finish and coated with white paint (typewriter correction fluid) in order to facilitate crack length determination.

The ambient temperature and relative humidity of the testing environment was 21°*C* (70°*F*) and 55% respectively.

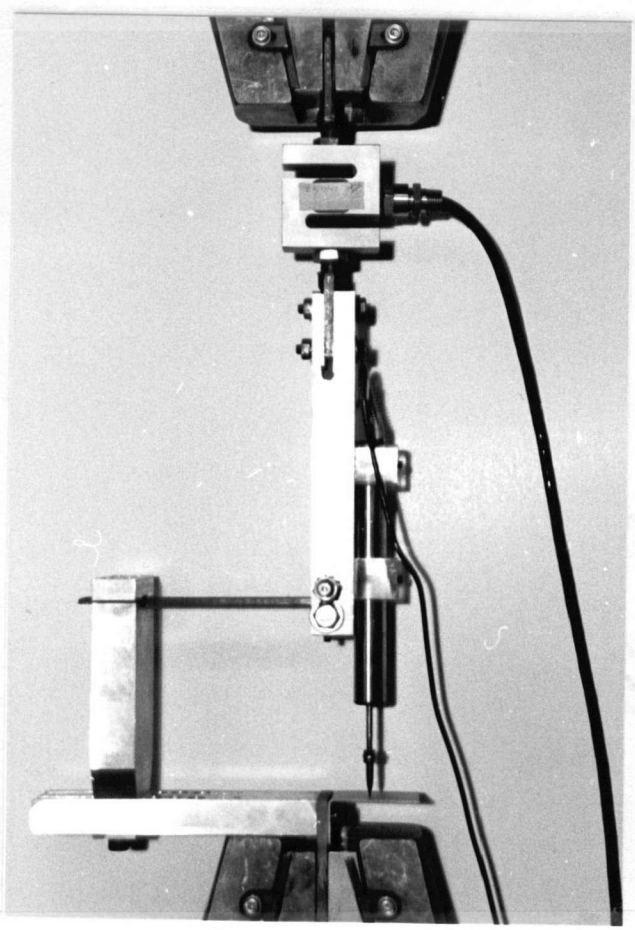

Figure 4.1 ENCB fatigue test apparatus.

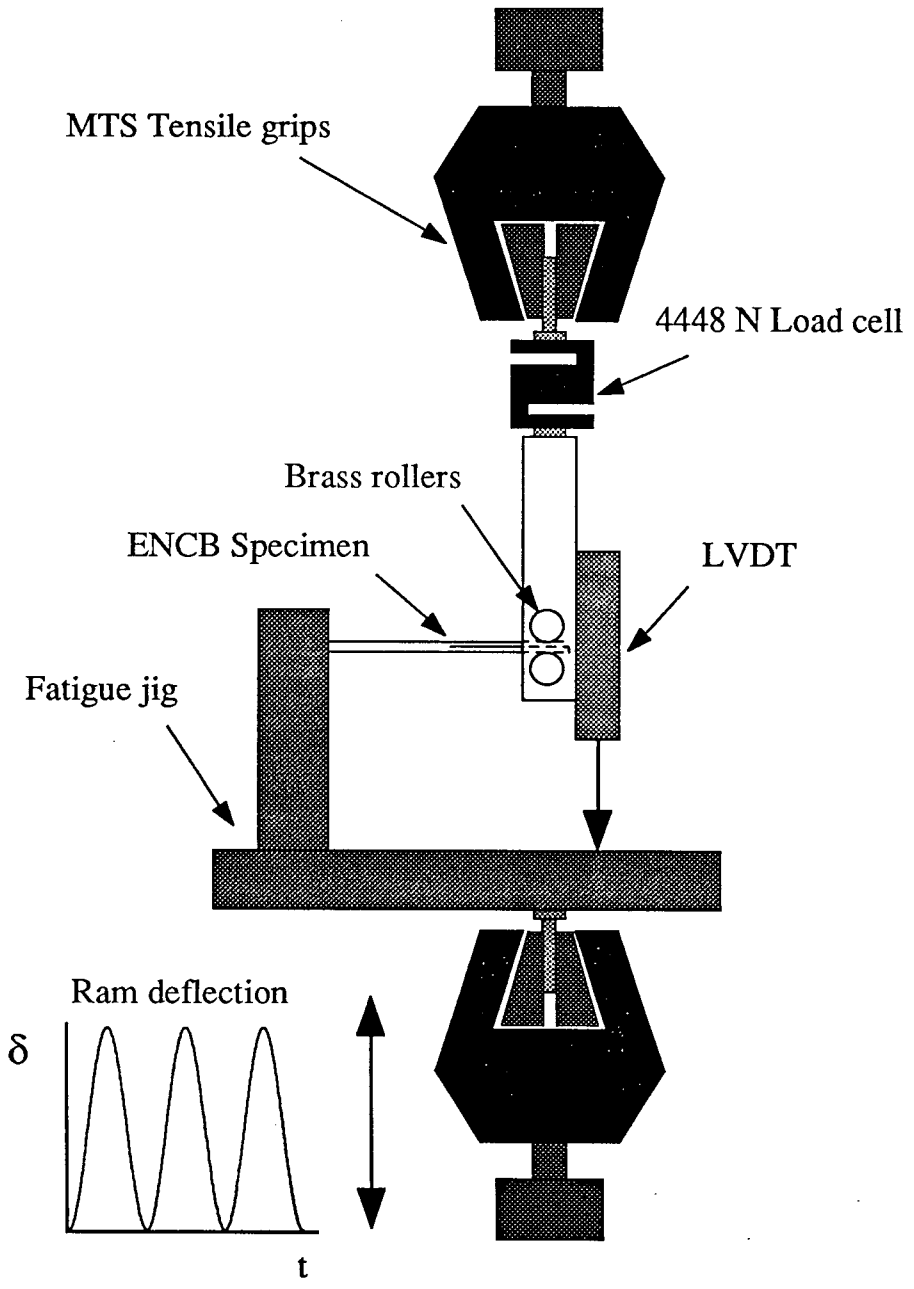

Figure 4.2 Schematic of ENCB fatigue test apparatus.

4.2 Data Reduction Techniques

4.2.1 Validity of Beam Theory

Preliminary experiments were performed to establish the validity of the ENCB beam theory compliance expression presented as equation (3.1). Two specimens were subjected to a loading regime which consisted of constant amplitude cycling at a frequency of 1 Hz of sufficient magnitude and duration to grow the delamination a distance of 5 mm. Three slow ramp cycles at a frequency of 0.2 Hz were then applied and the load and deflection data from each cycle were captured by the program and stored on hard disk. The compliance for that crack length was determined from the average of the linear regression coefficients fit to the three deflection versus load plots. An overload block of no more than 10 cycles at 1 Hz was then applied to just slightly advance the delamination approximately 1 mm. The delamination was grown in this manner through a total distance of 50 mm. This produced a series of fringes on the fracture surface as shown schematically in Figure 4.3, each of which could be associated with a particular compliance measurement and crack length. Upon completion of the preliminary fracture test, the specimen was separated into two halves and the crack lengths corresponding to each visible fringe were measured from the fracture surface.

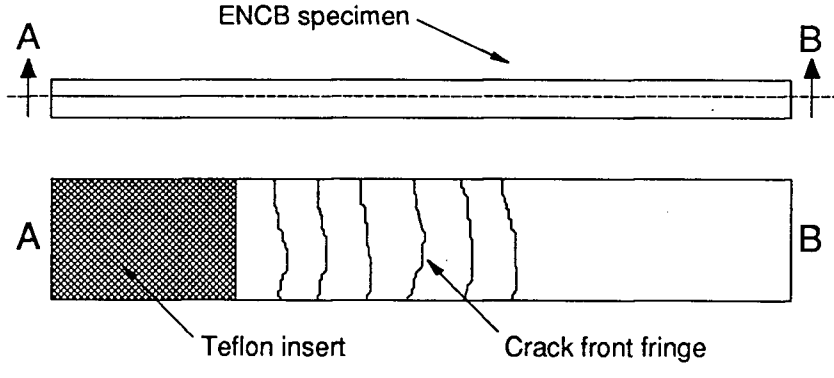

Figure 4.3 Schematic of fracture surface crack fringes.

Figure 4.4, which shows a plot of the measured compliances versus the term L^3+3a^3, establishes the validity of equation (3.1) as excellent linear agreement is obtained for the data. Extensive use was made of this linear relationship in the determination of crack lengths during subsequent fatigue testing. This approach will be presented in a forthcoming section.

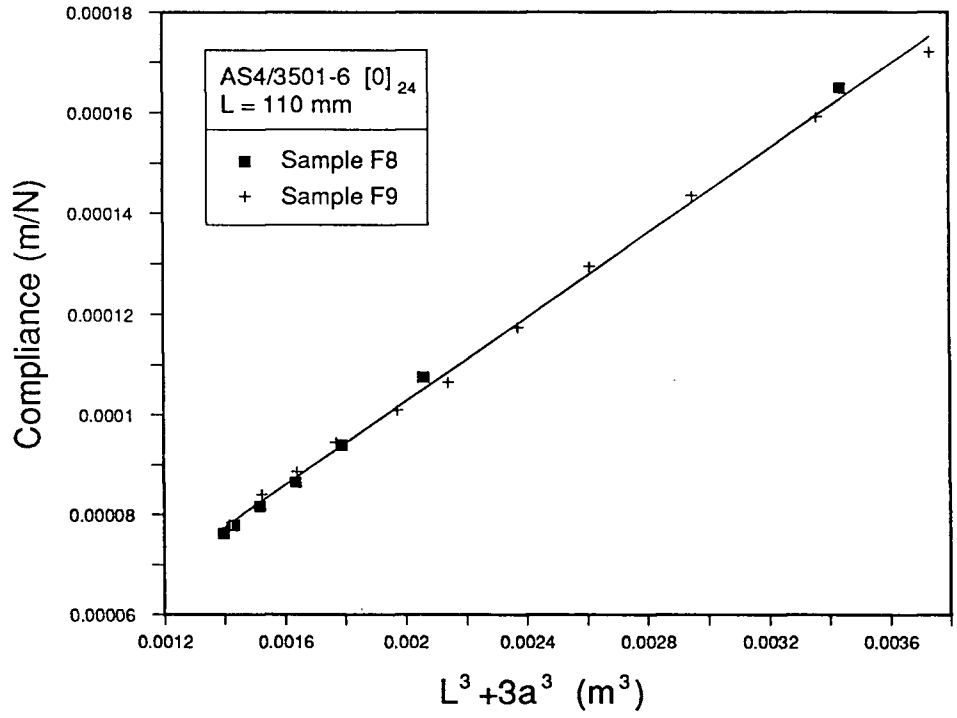

Figure 4.4 Relationship between ENCB specimen compliance and crack length.

As a further check of beam theory, the flexural modulus, E was calculated from the slope of the compliance calibration curve (equation (3.1)) obtained for each fatigue specimen (see Table 4.1). For comparison, an independently determined value of flexural modulus for this material is 131 GPa [35].

Table 4.1 Experimentally inferred flexural modulus.

Specimen	Modulus,E (GPa)
F16	127
F17	128
F18	127
F19	116
F20	129

4.2.2 Nonlinear Effects

During the initial stages of testing, evidence of a certain degree of nonlinearity was observed in the load-deflection behaviour of the ENCB specimen. Figure 4.5 shows an example in which the response is nonlinear at high applied deflections. Notice also that some hysteresis exists as the unload portion of the curve deviates slightly from the load-up curve.

Other researchers [36-39] have observed similar nonlinear mode II behaviour and numerous mechanisms have been proposed. In toughened composites (i.e. composites containing tougher thermoplastic resins), the observed nonlinearities have been attributed to a combination of slow stable crack growth preceding unstable crack growth and material inelastic behaviour in the process zone around the crack tip.

The carbon/epoxy composite tested in the present work is an inherently brittle system and hence, little matrix yielding is expected at the crack tip. Furthermore, the unloading curve returns to the origin. A permanent set, which is a definite indication of material inelastic behaviour, is absent from all the load-deflection curves obtained during testing in this work. The nonlinear behaviour observed here is very likely due to the large applied specimen

deflection, especially as it indicates a stiffening of the specimen. In addition, the hysteresis loop evident in Figure 4.5 is perhaps representative of the energy absorbed in the form of friction between the delaminated surfaces.

Figure 4.6 shows the load-deflection plot obtained from the same specimen as in Figure 4.5 but at a lower applied deflection. There is no evidence of hysteresis and the response is linear. Thus, during fatigue testing, care was taken to ensure that the compliance measurements were obtained from linear load-deflection plots. Even in instances where nonlinearity was unavoidable, particularly at longer crack lengths, the compliance was still obtained from the linear portion of the curves.

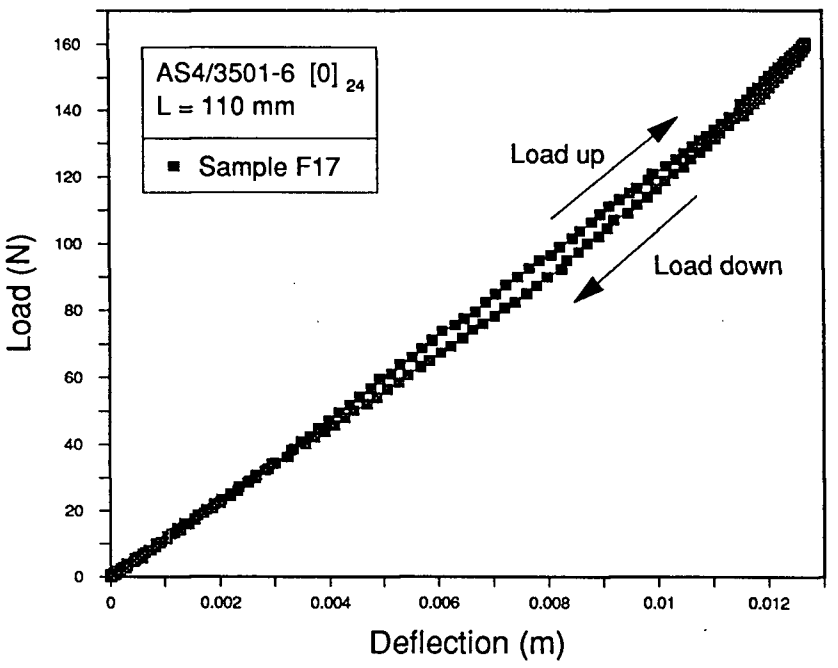

Figure 4.5 Typical ENCB load-deflection curve for high applied deflections.

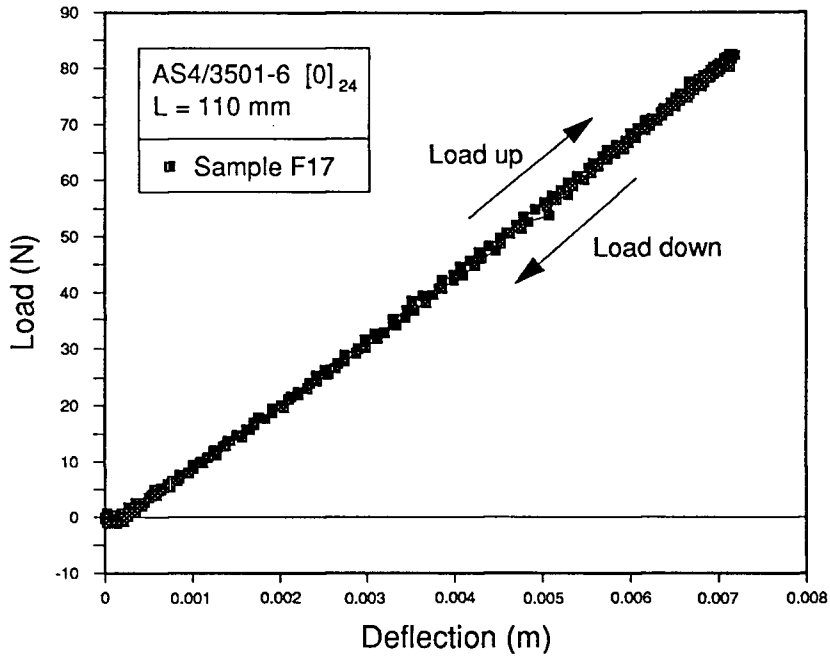

Figure 4.6 Typical ENCB load-deflection curve for low applied deflections.

4.2.3 Fatigue Characterization

With the widespread introduction of composite materials into structures subjected to cyclic loads, it is surprising to discover that to date there is no recommended procedure for cyclic delamination characterization. Recently, a round robin test program was established to develop standards for mode I and mode II static fracture toughness measurements [29]. Testing standards for fatigue characterization are being developed in a similar manner for the near future. In light of this, the approach taken in the current investigation was adapted from experimental procedures considered elsewhere in the literature [25-30,36-39].

The ENCB specimen was cycled at a specified R-ratio until the crack advanced approximately 0.5-1 mm as determined visually with the optical travelling microscope. A compliance measurement consisting of three single load-deflection data logging cycles was then

taken and the total number of cycles corresponding to the crack growth increment was recorded. The R-ratio definition was modified to reflect the fact that all specimens were cycled under deflection control, i.e.

$$R = \frac{\delta_{min}}{\delta_{max}} \tag{4.1}$$

Crack lengths were determined from a compliance calibration curve of a form similar to Figure 4.4 but specific to each specimen. This curve was generated for each fatigue specimen by first matching initial and final compliance values to initial and final crack lengths measured from the fracture surface at the completion of the fatigue test. These two pairs of points were substituted into equation (3.1) and the two unknown terms, C_o and $1/(2Ebh^3)$ were evaluated. The crack length corresponding to each periodic compliance measurement was then determined from this expression.

There are several advantages to using a compliance calibration curve over taking direct visual measurements to determine crack lengths. Clearly, variations in the crack front through the width of the specimen cannot be accounted for by crack length measurements taken from the specimen edge. The compliance method accounts for any crack front deviation in an averaged sense. This may not have been significant in the current investigation as variations in the crack front only amounted to less than 10% in all samples tested. In addition, the compliance method may be easily adapted to a completely automated test procedure. A comparison of the two techniques for two specimens is shown in Figure 4.7. In both instances, the compliance method matches the visual crack measurements quite effectively.

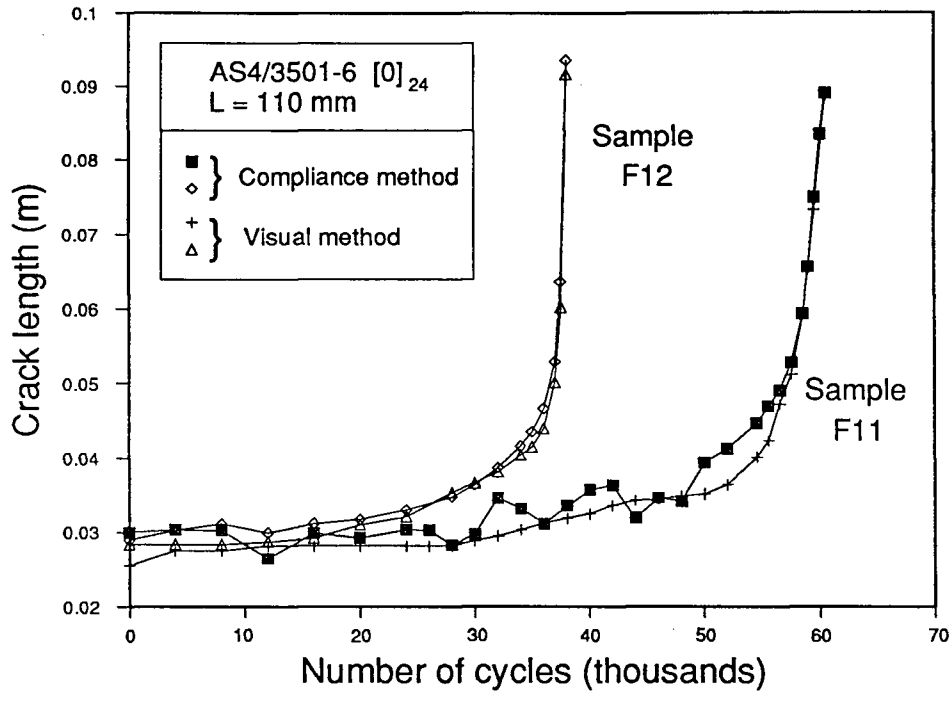

Figure 4.7 Comparison of compliance method and visual method for crack length determination of two specimens.

Earlier it was pointed out that fatigue crack growth in metals is characterized by relating the growth rate, da/dN to the cyclic stress intensity factor range, ΔK. For composite materials, mode II delamination growth is related to the cyclic strain energy release rate range, ΔG_{II} by an expression of the form

$$\frac{da}{dN} = A(\Delta G_{II})^n \tag{4.2}$$

where A and n are constants determined from a log-log plot of da/dN versus ΔG_{II} and where

$$\Delta G_{II} = G_{II\max} - G_{II\min} \tag{4.3}$$

The delamination growth rates, da/dN were determined by calculating the slope of the straight line connecting two adjacent points from curves of inferred crack length (calculated from compliance measurements) versus number of cycles. This adjacent point approximation has been verified to be reasonable if the delamination length increments are small [29].

The zero and positive shear ($R \geq 0$) cyclic strain energy release rate range is derived from equations (3.3) and (4.3) and is defined as

$$\Delta G_{II} = \frac{9a^2(\delta_{max}^2 - \delta_{min}^2)\left(1 - \frac{C_o}{C}\right)}{2b(L^3 + 3a^3)C} \tag{4.4}$$

The determination of ΔG_{II} for the negative shear ($R < 0$) case however, is not intuitively obvious. For example, major differences seem to exist in the literature in the definition of ΔG_{II} at $R = -1$ [25,40]. One method involves replacing the $(\delta_{max}^2 - \delta_{min}^2)$ term in equation (4.4) with $2\delta_{max}^2$ [40]. A common approach is to consider ΔG_{II} at $R = -1$ equal to ΔG_{II} at $R = 0$, i.e. consider δ_{min} equal to zero in equation (4.4) for both cases [25]. This seems to be a reasonable assumption due to the nature of the relationship between applied deflection and strain energy release rate range. Since G_{II} is proportional to the square of δ, it is positive for both positive and negative shear loadings. For $R = -1$ for example, two maxima in G_{II} of equal value occur during each cycle; however, for $R = 0$, there is only one maximum per cycle (see Figure 4.8). In order to eliminate this two-to-one maxima effect in the current work, all negative shear crack growth rates were divided by two. Strain rate effects were minimized by setting the frequency at 1 Hz for the $R \geq 0$ tests and 0.5 Hz for the $R < 0$ tests.

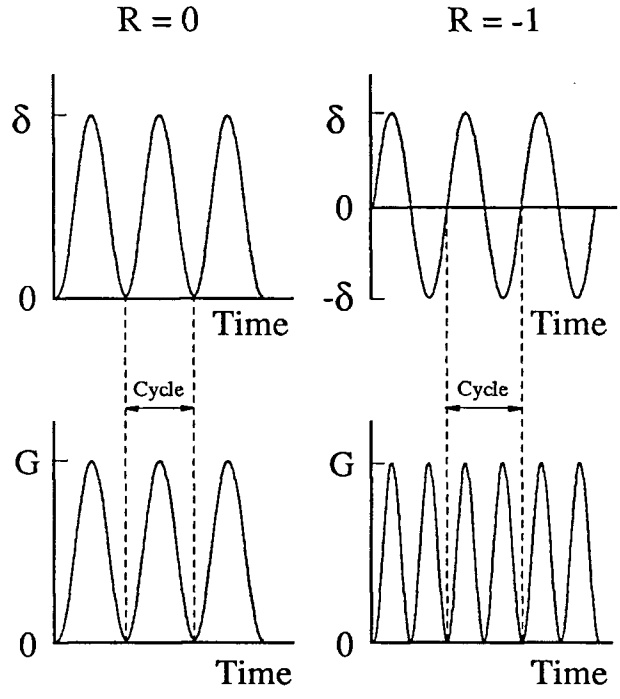

Figure 4.8 Relationship between deflection and strain energy release rate for $R = 0$ and $R = -1$.

An additional complication arises for negative shear tests where R is not equal to -1. When $R = -0.50$ for example, (i.e. $K_{min} = 0.5K_{max}$), the two G_{II} peaks produced in every cycle are unequal. In this instance one can consider a single $R = -0.50$ cycle as being a superposition of two $R = -1$ half-cycles as shown in Figure 4.9. Notice that the maximum applied deflection of the first $R = -1$ half-cycle is twice that of the second $R = -1$ half-cycle. This translates to a factor of four difference in G_{II}. It would seem logical therefore, to consider the first half-cycle as being the controlling cycle for crack growth. Thus, ΔG_{II} was calculated from equation (4.4) with δ_{min} equal to zero and δ_{max} equal to the maximum deflection of the first half-cycle.

For convenience, Figure 4.10 shows a simplified schematic overview of the fatigue data reduction procedure. Any deviations from the procedure outlined here will be dealt with in subsequent sections.

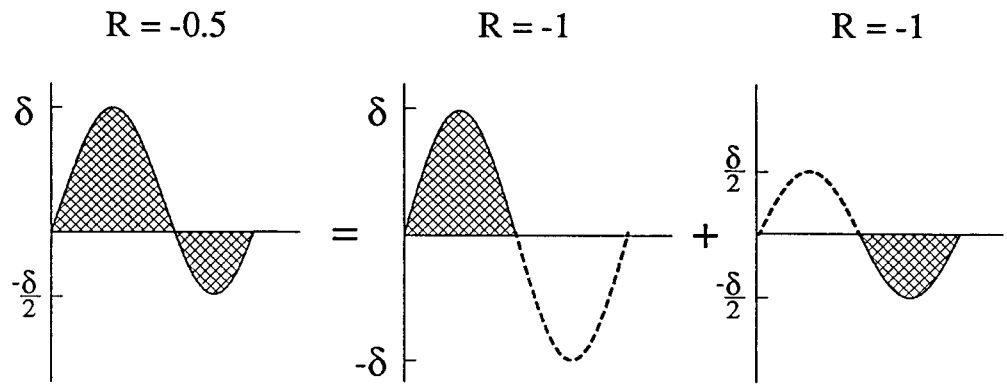

Figure 4.9 The generation of an $R = -0.50$ cycle from the superposition of two $R = -1$ half-cycles.

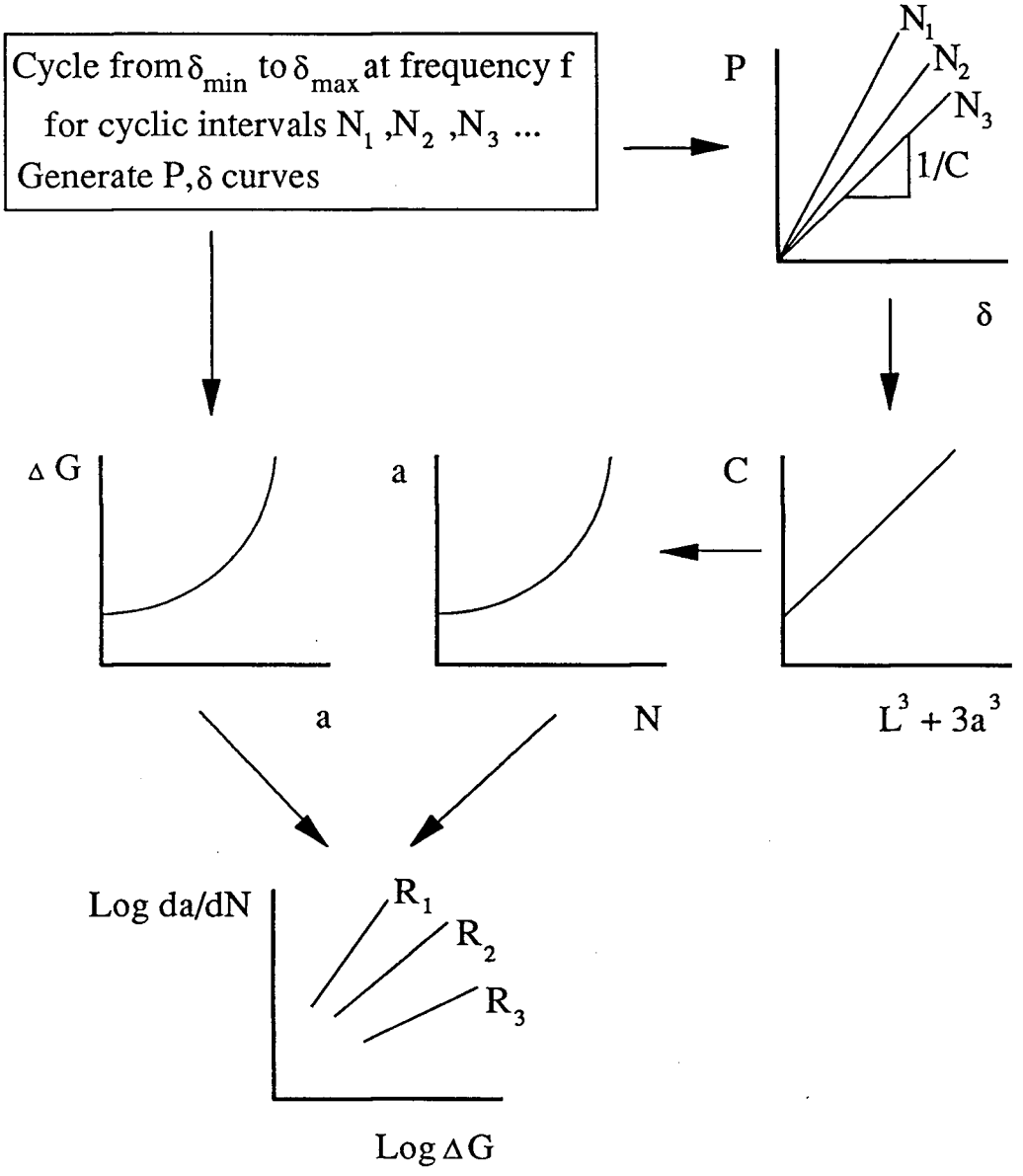

Figure 4.10 Fatigue data reduction schematic.

5 FATIGUE RESULTS

5.1 Reliability Tests

Prior to examining the effect of R-ratio on delamination growth rates, two specimens were tested at $R = 0$ in order to compare the results with previously published data. These preliminary experiments served as a reliability check for the fatigue testing equipment and data reduction procedure.

The crack growth rates for these reliability tests were determined from three point incremental linear regressions along the crack growth curves. As shown in Figure 5.1, data from the two specimens was combined, and plotted as a function ofΔG_{II}, using logarithmic scales for both axes. A comparison is made with the results presented in Ref [25] over the same ΔG_{II} range. Although some scatter in the growth behaviour is evident, the curve fit agrees with the published results. The present values of the crack growth parameters, A and n of 5.32×10^{-16} and 5.17 are similar to those obtained in Ref [25], (2.23×10^{-17} and 5.79 respectively). It should be noted that the experimental work in Ref [25] was conducted at the same R-ratio ($R = 0$) but at a higher frequency (2 Hz). In addition, although the resin system was the same, the reinforcement was provided by first generation AS1 fibres, rather than the AS4 fibres used in the current work. Further comparison with work carried out by other researchers is difficult due to the scarcity of published data on mode II fatigue delamination (see Table 2.1).

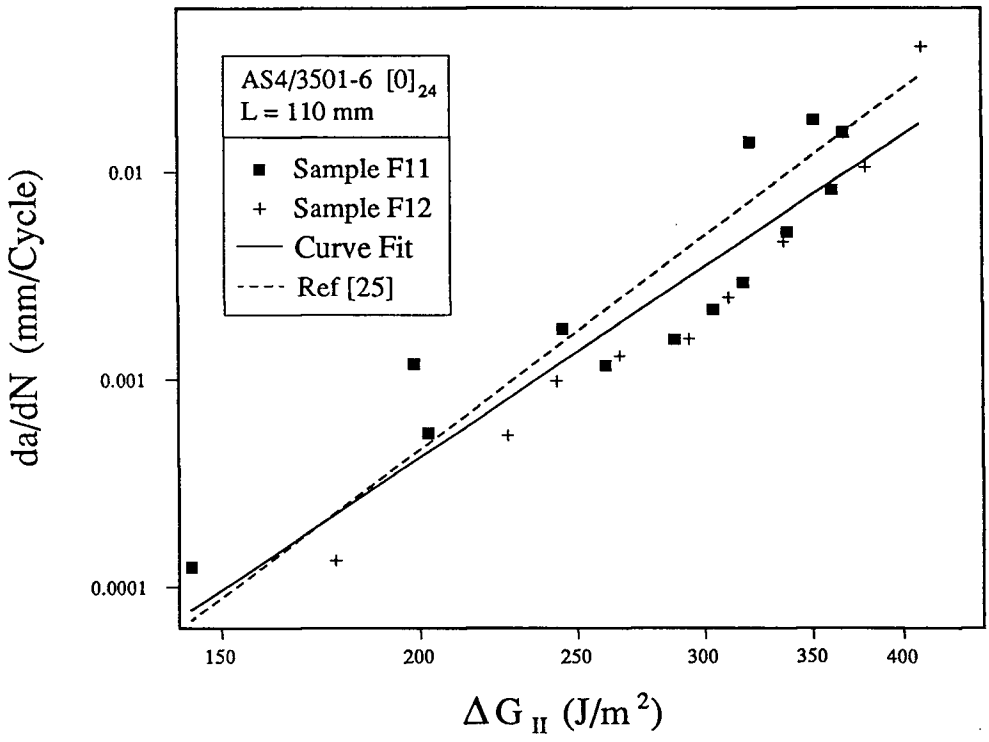

Figure 5.1 Mode II fatigue crack growth rate data from reliability tests.

5.2 Effect of R-Ratio

5.2.1 Initial Observations

In order to devise an efficient testing schedule, it was first necessary to determine the general crack growth rate trend as a function of increasing R-ratio. A sample was subjected to a constant ΔG_{II} cyclic loading block sufficient to provide a growth rate of *1 mm* in *1000* cycles at $R = 0$. Based on the results obtained during the reliability tests (see Figure 5.1), a ΔG_{II} of *250* J/m^2 was chosen.

The sample was cycled at $R = 0$ for *1000* cycles to give an initial growth of approximately *1 mm*. The maximum cyclic deflection required to maintain a ΔG_{II} of *250* J/m^2 was *11 mm*.

The R-ratio was then changed to $R = 0.50$ but ΔG_{II} was kept constant at $250\ J/m^2$. The crack length was measured optically with the travelling microscope every *200 cycles* in order to obtain the new growth rate. No growth was observed for the delamination under these conditions after as many as *4000* cycles.

These preliminary results indicated that either the R-ratio affects the crack growth rate differently than in metals, or that crack retardation was occuring due to some interaction between the $R = 0$ and $R = 0.50$ blocks. Generally, the application of an overload during the cycling of materials which exhibit ductility at the crack tip results in a decrease in crack velocity until the crack grows through the plastic zone created by the overload. The decrease in crack velocity is related to the residual compressive stress field at the crack tip due to the overload [9,10].

The possibility of crack retardation was investigated next by reducing the R-ratio to $R = 0$ and monitoring the growth rate. After *1000* cycles the crack had again grown approximately *1 mm*, indicating that the behaviour was due to the change in R-ratio. The observed absence of any retardation effect is in agreement with a previous study [41] conducted on similar material which claimed that there is insufficient plasticity at the crack tip to give a measurable effect. The epoxy resin, which is by nature a brittle material, has a characteristically small plastic zone size. In addition, the presence of closely packed fibres further discourages any permanent deformation.

The above results seemed to indicate that an increase in R-ratio would give a decrease in crack growth rate at a constant level of ΔG_{II}. Therefore, only a limited range of R-ratios, bounded by a maximum value of $R = 0.50$, could realistically be examined. Instead of cycling at a constant ΔG_{II}, which scales as $\delta_{max}^2 - \delta_{min}^2$, cycling was carried out at a constant $\Delta\delta = \delta_{max} - \delta_{min}$, which is proportional to ΔK_{II}. Additional testing indicated that a $\Delta\delta$ of *6 mm* would provide

reasonable growth rates for a range of R-ratios from $R = 0$ to $R = 0.50$. Values of R-ratio greater than $R = 0.50$ resulted in growth rates rapidly approaching single cycle failure for a $\Delta\delta$ of *6 mm.*

Each specimen was subjected to a series of alternating R-ratios resulting in small crack growth increments (*0.5-1 mm*) such that the growth rate curves were generated in a step-wise manner. For example, consider the data generated for specimen F16 in Appendix A. Specimen F16 was subjected to fatigue cycling at R-ratios of *0, 0.25* and *0.50* over a crack length range of *47.25 mm.* Each crack growth increment of approximately *0.5-1 mm* at $R = 0$ was followed by a similar increment but at $R = 0.50$ which was subsequently followed by another increment at $R = 0$. This procedure was repeated until it was determined that further testing at $R = 0.50$ would result in catastrophic failure. A new, lower R-ratio was then chosen, i.e. $R = 0.25$ and testing was resumed by alternately cycling at $R = 0$ and $R = 0.25$. The effect of R-ratio on delamination growth rate could therefore be monitored while testing was in progress. This also resulted in the effective use of the large range of crack lengths possible in each ENCB specimen.

5.2.2 Fatigue Crack Growth Rate Laws

In the current investigation, R-ratios ranging from $R = -1$ to $R = 0.50$ were examined. The fatigue data for all specimens tested is presented in Appendix A. The crack growth rate is plotted as a function of ΔG_{II}, $G_{II\max}$ and ΔK_{II} in log-log coordinates as shown in Figures 5.2 - 5.4. The data obeys a relationship of the form of equation (4.2). Values for ΔK_{II} were obtained from the following expression:

$$\Delta K_{II} = K_{II\max} - K_{II\min} \tag{5.1}$$

where $K_{II\,max}$ and $K_{II\,min}$ were obtained from experimentally determined values of $G_{II\,max}$ and $G_{II\,min}$, and the orthotropic equivalent to $K^2 = EG$, as the latter is only valid for isotropic materials. For the mode II loading case [42]

$$K_{II}^2 = E'' G_{II} \tag{5.2}$$

where

$$E'' = \frac{\sqrt{2}}{a_{11}}\left[\sqrt{\frac{a_{33}}{a_{11}}} + \frac{2a_{13} + a_{66}}{2a_{11}}\right]^{-1/2} \tag{5.3}$$

and where the a_{ij} terms are textbook [43] compliance values for the material. The value for E'' calculated from equation (5.3) was *53.4 GPa*. Note that E'' in equation (5.2) differs in value from E', which is used in $K_I^2 = E' G_I$, and is generally found in the literature. Therefore, equation (5.3) is correct.

The fatigue parameters, A and n were determined by a linear regression fit to the experimental data for each R-ratio based on ΔG_{II}, $G_{II\,max}$ and ΔK_{II} and are listed in Tables 5.1 - 5.3. Subscripts G, GM and K were used with the fatigue parameters A and n in order to differentiate between the ΔG_{II}, $G_{II\,max}$ and ΔK_{II} correlation respectively. Data points not lying within a reasonable scatter band based on a visual estimation were censored from the linear regression fit.

Over the range of ΔG_{II} tested, there appears to be a large dependence of crack growth rate on R-ratio (see Figure 5.2). At a constant value of ΔG_{II}, as the R-ratio increases from $R = -1$ to $R = 0.50$, the crack growth rate decreases. A similar result was reported in Ref [25] under nearly identical testing conditions for just two R-ratios (R = 0 and R = -1). This is also consistent with the initial results presented in Section 5.2.1 where no growth was observed when the R-ratio

was increased from $R = 0$ to $R = 0.50$. If the $R = 0$ curve in Figure 5.2 were extended to a ΔG_{II} of $250\ J/m^2$, then the expected growth rate would lie roughly between 10^{-3} and 10^{-2} *mm/cycle*. At the same level of ΔG_{II}, the growth rate at $R = 0.50$ should be approximately two decades lower.

The fan-shaped appearance of the R-ratio curves in Figure 5.2 is due to the effect of R-ratio on both fatigue parameters, A_G and n_G. As the R-ratio increases, the slope, n_G increases whereas the intercept, A_G decreases (see Table 5.1). This effect is in agreement with the results presented in Ref [25] where n_G increases from *3.87* to *5.87* and A_G decreases from 1.01×10^{-12} to 2.23×10^{-17} as the R-ratio changes from $R = -1$ to $R = 0$. Interestingly, the same trend is observed in the mode III characterization of a similar material [31].

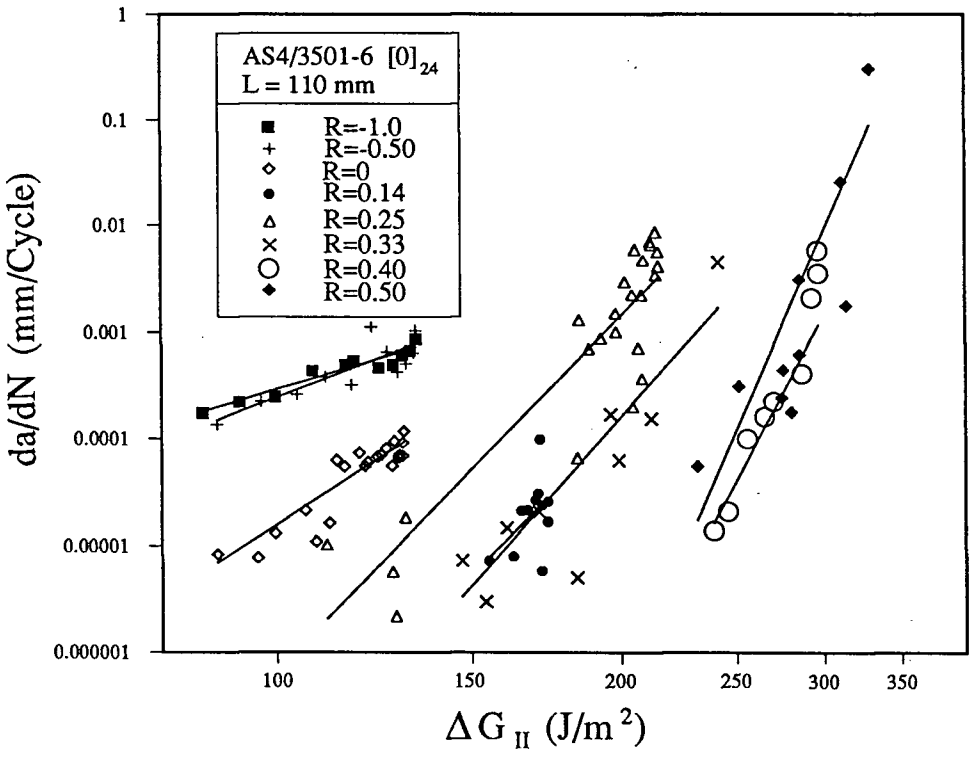

Figure 5.2 Mode II fatigue crack growth rate data based on ΔG_{II}.

Table 5.1 Summary of fatigue parameters based on ΔG_{II}.

R-ratio	Intercept A_G	Slope n_G	Correlation Coefficient	Data Points	Frequency (Hz)
-1	1.08×10^{-10}	3.21	0.919	11	0.5
-0.50	1.56×10^{-12}	4.09	0.731	11	0.5
0	1.92×10^{-19}	6.96	0.897	19	1.0
0.14	1.27×10^{-24}	8.90	0.666	11	1.0
0.25	5.41×10^{-29}	11.1	0.813	24	1.0
0.33	2.21×10^{-32}	12.1	0.900	8	1.0
0.40	8.22×10^{-45}	16.8	0.941	6	1.0
0.50	2.95×10^{-53}	20.5	0.825	8	1.0

Figure 5.2 includes several sets of curves for which the effect of R-ratio is nearly identical. The negative shear data, $R = -1$ and $R = -0.50$ are one set and the highly positive shear data, $R = 0.40$ and $R = 0.50$ are another. The intermediate positive shear data, $R = 0$ to $R = 0.33$ constitute a third set. These three sets show significant differences in A_G and n_G values as R-ratio increases. Since the R-ratio represents a measure of the level of mean applied deflection, it is not surprising that in instances where the R-ratio is similar in magnitude, the resulting crack growth rates are virtually identical. Larger differences in R-ratio, and hence mean deflection, are required to make the effect more pronounced.

Intuitively, as the mean deflection level increases with R-ratio, one would expect a corresponding increase in growth rate. The increase in slope, n_G therefore is quite understandable. However, the intercept, A_G decreases with R-ratio and the net effect is a *decrease* in growth rate, opposite to what is expected.

The log-log plot of crack growth rate as a function of $G_{II\,max}$ presented in Figure 5.3 shows trends similar to those found in Figure 5.2. By plotting the growth rate data as a function of

$G_{II\,max}$, the effect of R-ratio is visually intensified as the curves are offset slightly with respect to Figure 5.2. In addition, the fan-shaped nature of the curves has slightly more significance when plotted versus $G_{II\,max}$. Although the R-ratio curves in both figures may be extended to a common intersection point, the intersection point in Figure 5.3 is nevertheless more meaningful as it represents an asymptote to the critical value of strain energy release rate, G_{IIc}, for this material. Intersection occurs at a $G_{II\,max}$ of approximately *500 J/m²* in Figure 5.3. Values for G_{IIc} quoted in the literature range from *450 - 630 J/m²* [e.g. 26,36,38].

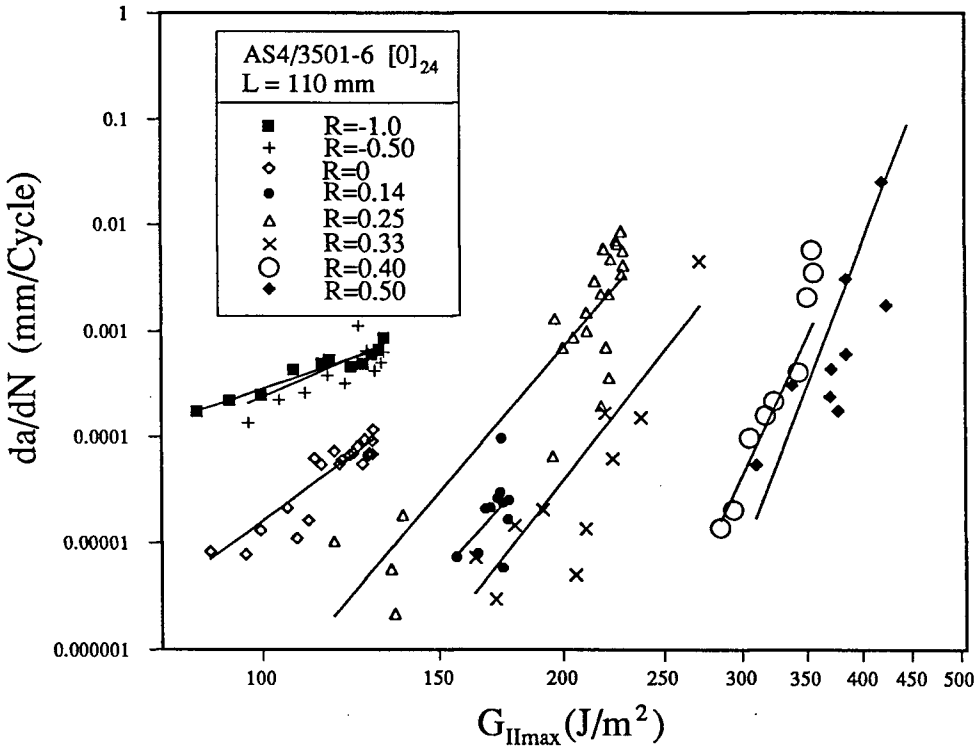

Figure 5.3 Mode II fatigue crack growth rate data based on G_{IImax}.

Table 5.2 Summary of fatigue parameters based on $G_{II\,max}$.

R-ratio	Intercept A_{GM}	Slope n_{GM}	Correlation Coefficient	Data Points	Frequency (Hz)
-1	1.08×10^{-10}	3.21	0.919	11	0.5
-0.50	1.56×10^{-12}	4.09	0.731	11	0.5
0	1.92×10^{-19}	6.96	0.897	19	1.0
0.14	1.05×10^{-24}	8.91	0.666	11	1.0
0.25	2.65×10^{-29}	11.1	0.813	24	1.0
0.33	5.32×10^{-33}	12.1	0.900	8	1.0
0.40	4.42×10^{-46}	16.8	0.941	6	1.0
0.50	8.18×10^{-56}	20.5	0.825	8	1.0

Crack growth rate data plotted as a function of the stress intensity range ΔK_{II} (derived from equations (5.1) - (5.3)) is plotted in log-log coordinates and shown in Figure 5.4. Excluding the negative shear data, there is a dependence of the growth rate on R-ratio; however, the effect is opposite to that seen by either the ΔG_{II} and $G_{II\,max}$ approach of Figures 5.2 and 5.3. At a constant level of ΔK_{II}, as R-ratio increases from $R = 0$ to $R = 0.50$, the growth rate increases (with the exception of the misbehaved $R = 0.14$ and $R = 0.40$ data). It is interesting that the data is less widely separated in ΔK_{II} space compared to ΔG_{II} or G_{IImax} space. As a result, the trend is less convincing, but nevertheless the opposite of Figures 5.2 and 5.3.

The results of Figure 5.4 are in agreement with the mean stress argument used with metals and many isotropic materials. The increase in R-ratio implies a higher mean stress at the crack tip resulting in a shorter life, i.e. a higher growth rate. Work carried out on a slightly different carbon/epoxy system in mode I shows this trend [28]. The effect of R-ratio on crack growth rate is reversed when the comparison is switched from a strain energy release rate approach to a stress intensity approach. It is interesting to note that the effect of R-ratio on the parameters A_K and n_K is the same as on A_G and n_G. As before, when the R-ratio increases, the slope, n_K

increases and the intercept, A_K decreases (compare Table 5.3 with Table 5.1). These results are more effectively visualized in Figures 5.5 and 5.6 which show plots of $n_{G,K}$ and $A_{G,K}$ versus R-ratio respectively.

Note that the constant, A_G is more sensitive to changes in R-ratio. The net effect of the decrease in A_G in Figure 5.6 and the increase in n_G in Figure 5.5 is a reduction in crack growth rate as R-ratio increases for a constant ΔG_{II}. However, for a constant ΔK_{II}, the net effect of the reduction in A_K and increase in n_K is an increase in crack growth rate. This reconciles the contradictory growth rate trends shown in Figures 5.2 and 5.4.

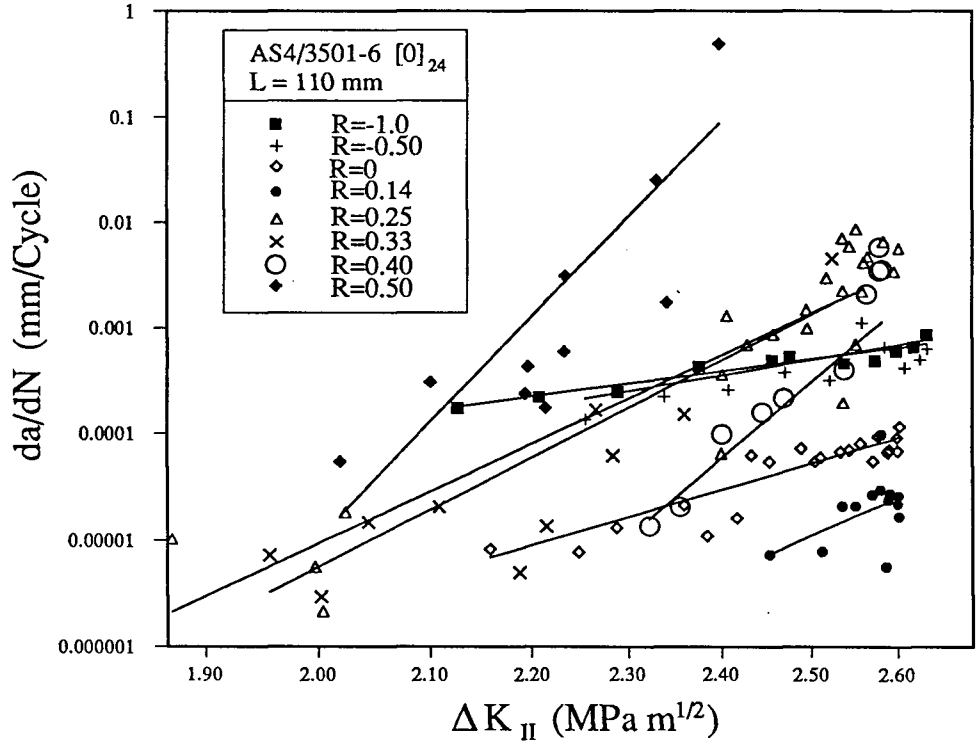

Figure 5.4 Mode II fatigue crack growth rate data based on ΔK_{II}.

Table 5.3 Summary of fatigue parameters based on ΔK_{II}.

R-ratio	Intercept A_K	Slope n_K	Correlation Coefficient	Data Points	Frequency (Hz)
-1	1.40×10^{-6}	6.42	0.919	11	0.5
-0.50	2.73×10^{-7}	8.18	0.731	11	0.5
0	1.58×10^{-10}	13.9	0.897	19	1.0
0.14	4.36×10^{-12}	17.8	0.662	11	1.0
0.25	2.23×10^{-12}	22.1	0.812	24	1.0
0.33	3.31×10^{-13}	24.2	0.901	8	1.0
0.40	3.85×10^{-17}	33.5	0.941	6	1.0
0.50	2.65×10^{-17}	41.0	0.826	8	1.0

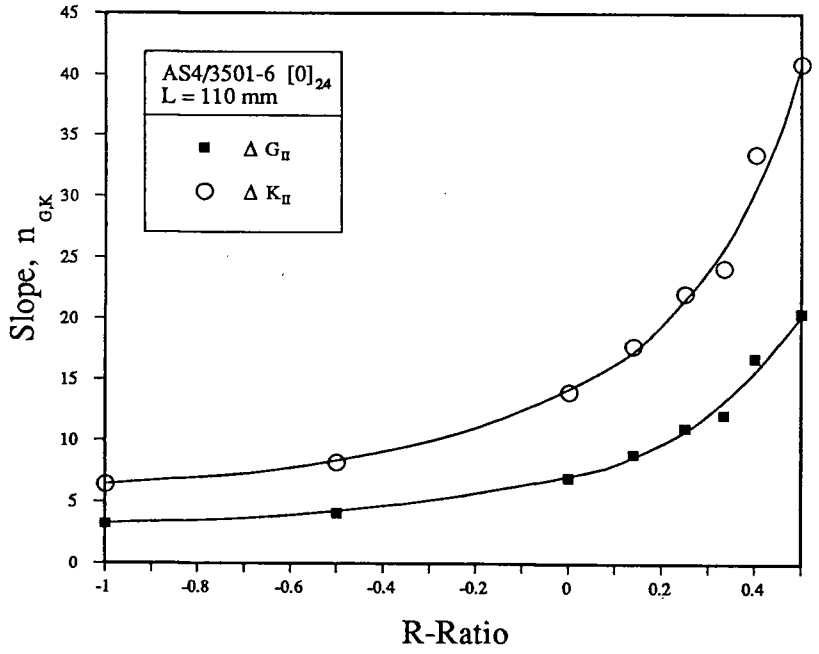

Figure 5.5 Experimental variation of slope, $n_{G,K}$ with R-ratio.

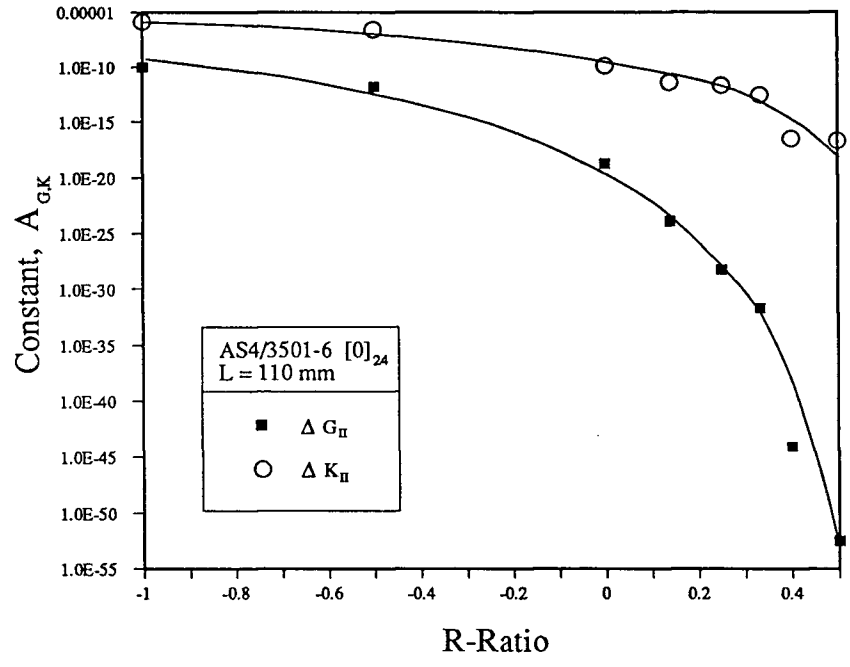

Figure 5.6 Experimental variation of constant, $A_{G,K}$ with R-ratio.

In Figure 5.5 a factor of two difference exists in the values of n_G and n_K due to the manner in which ΔK_{II} and ΔG_{II} are defined. The relatively high values of n_G and n_K obtained for this carbon/epoxy system, particularly at high R-ratios is most significant. Typical values of n_K for fatigue crack growth in aluminum and steel range from only *1.5* to *2.5* [44]. A high value of n_K (or n_G) implies that a small change in applied deflection (or load) would lead to a large change in crack growth rate in composites. Fatigue crack growth in composites is therefore more sensitive to errors in design load than are typical cracks in metallic structures. This result has been observed previously [e.g. 29-31,45]. In addition, this sensitivity is greater in brittle composites than in ductile composites [45]. As a result, the design of structural components based on a finite life approach against delamination would be a difficult undertaking with brittle matrix composites. Design alterations or analysis errors could result in a much shorter life than otherwise expected. For this reason, an alternative method involving an infinite life approach

has been proposed based on a no-delamination growth threshold, G_{th} [29,31,45]. Values for G_{th} are obtained by monitoring the number of cycles to delamination growth onset. It is assumed that if the delamination does not grow after 1 million cycles, the applied strain energy release rate is below the threshold value.

No attempt was made to determine the mode II threshold value of delamination growth, G_{IIth}, in the current study. However, the present results have some interesting implications for composite design based on an infinite life approach. It has been shown that an increase in R-ratio from $R = 0.10$ to $R = 0.50$ increases G_{IIth} by 43% [29]. Based on a strain energy release rate approach, this is consistent with the observation that as R-ratio increases, crack growth rate decreases. The stress intensity approach however, predicts the reverse of this, as shown earlier. It is therefore conceivable that results opposite to those obtained in Ref [29] may be generated. A situation may be envisaged whereby for an uncharacterized composite material system, G_{IIth} decreases as R-ratio increases, resulting in unexpected crack growth. It should be noted that the material system tested in Ref [29] was a toughened carbon composite. The implications for a brittle composite system are expected to be equivalent.

In an effort to simplify design considerations for fatigue crack growth in AS4/3501-6 carbon/epoxy composites, the current fatigue data was re-examined with emphasis placed on the complete characterization of the observed behaviour. Figures 5.5 and 5.6 provide an indication that the power law relationship is somewhat more complex than simply a slight modification of the Paris Law as presented in equation (4.2). The fatigue parameters $n_{G,K}$ and $A_{G,K}$ are unique functions of R-ratio. An expression relating these two parameters to R is obtained by plotting $n_{G,K}$ and $-log(A_{G,K})$ as a function of $(1-R)$ (which scales as the maximum stress) in log-log coordinates. It would be equally valid to plot the data versus $(1+R)/(1-R)$ which scales

as the mean stress. It is intuitively unclear as to why both approaches work. Nevertheless, Figures 5.7 and 5.8 indicate that a linear regression fit to the simpler *(1-R)* derivation is excellent. Over the entire range of R-ratios tested, the data based on ΔG_{II} yields the following results:

$$n_G = 7.53(1-R)^{-1.37} \tag{5.4}$$

$$A_G = 10^{-20.7(1-R)^{-1.24}} \tag{5.5}$$

On the other hand, the data based on ΔK_{II} yields:

$$n_K = 15.0(1-R)^{-1.37} \tag{5.6}$$

$$A_K = 10^{-9.72(1-R)^{-0.802}} \tag{5.7}$$

The following power law relationships are therefore established:

$$\frac{da}{dN} = 10^{-20.7(1-R)^{-1.24}} (\Delta G_{II})^{7.53(1-R)^{-1.37}} \tag{5.8}$$

$$\frac{da}{dN} = 10^{-9.72(1-R)^{-0.802}} (\Delta K_{II})^{15.0(1-R)^{-1.37}} \tag{5.9}$$

The effectiveness of the data fit is best judged by a comparison of the predicted crack growth derived from equations (5.8) and (5.9) and the actual experimentally measured growth rate. Figures 5.9 and 5.10 illustrate that virtually all the data lie within a scatterband centered about a line representing a slope of unity. Each R-ratio data set seems to have the correct slope, but deviations in the predicted growth rate as high as two decades are evident within the scatterband. A slope of unity merely reflects the excellent fit obtained in equations (5.4) and (5.6) for $n_{G,K}$ (see also Figure 5.7). The deviations in absolute values of predicted growth rate are due to the constant, $A_{G,K}$. Figure 5.8 shows that some scatter does exist in the linear fit which

yields equations (5.5) and (5.7). In addition, $A_{G,K}$ is very sensitive to errors in the experimental determination of R-ratio. This in turn leads to errors in the predicted growth rates. For example, at low values of R-ratio, an error in R of *0.01* results in a factor of *2* error in the predicted growth rate. For a difference of *0.1*, an error factor in excess of *400* occurs in the growth rate. This effect is even more significant at higher values of R-ratio. It would seem reasonable to expect small errors in R-ratio at the experimental level due to equipment fluctuations as a result of sudden voltage changes or hydraulic anomalies.

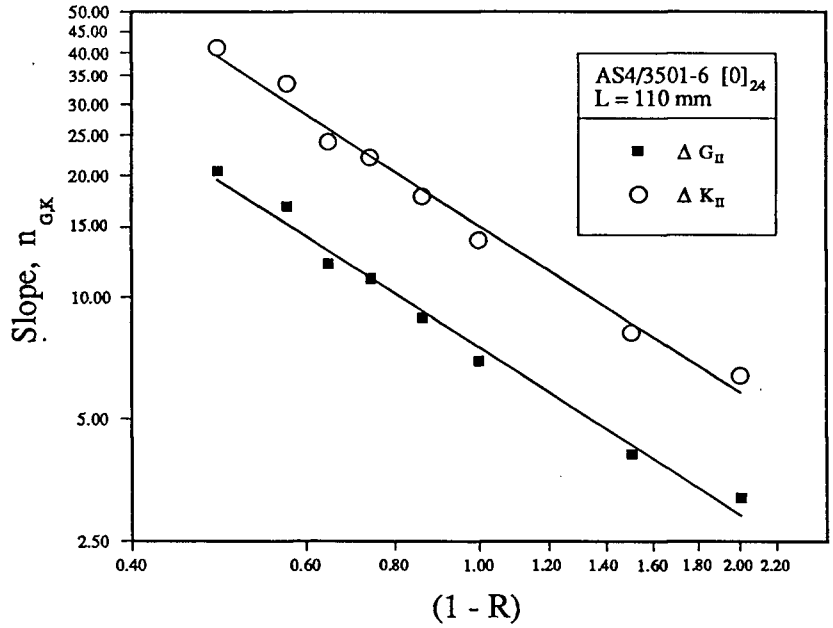

Figure 5.7 Experimental variation of slope, $n_{G,K}$ with (1-R) in log-log coordinates.

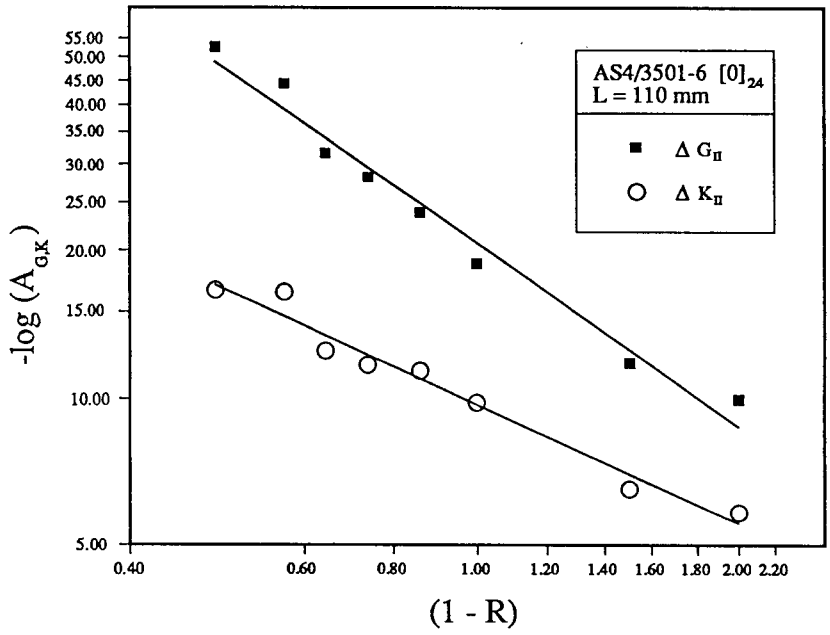

Figure 5.8 Experimental variation of constant, $A_{G,K}$ with (1-R) in log-log coordinates.

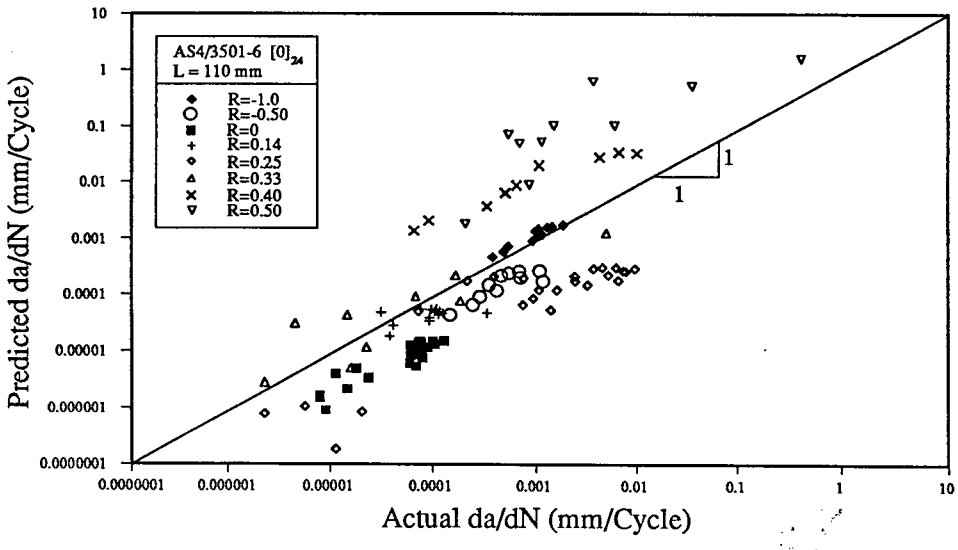

Figure 5.9 Predicted versus actual growth rate based on ΔG_{II} in log-log coordinates.

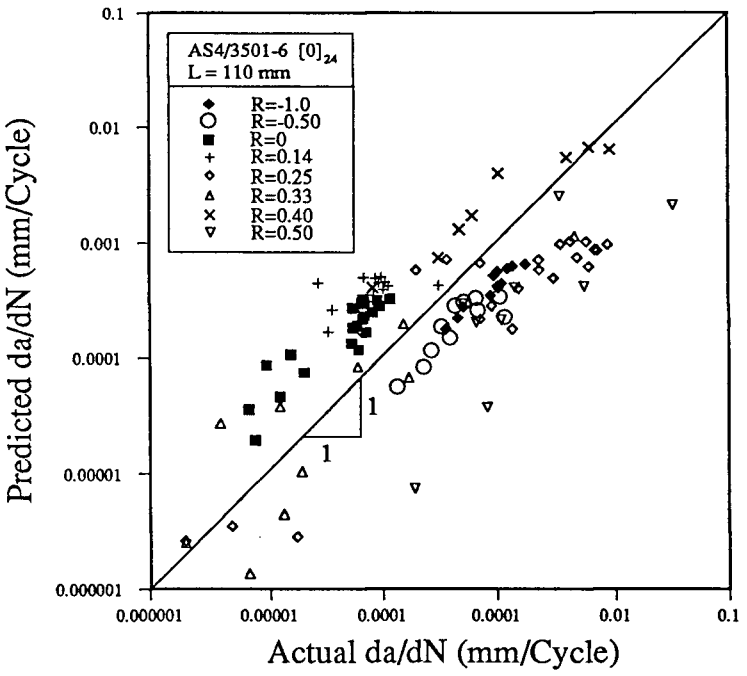

Figure 5.10 Predicted versus actual growth rate based on ΔK_{II} in log-log coordinates.

5.2.3 Time-at-Load Considerations

The effect of time-at-load was considered in an attempt to explain the behaviour of the fatigue parameters, $A_{G,K}$ and $n_{G,K}$ with changing R-ratio. Composite materials exhibit time dependent behaviour in instances where matrix contribution to loading capacity is significant [46].

A time-at-load approach considers the amount of time a specimen spends under constant load and the corresponding sub-critical crack growth. The total fatigue effect can therefore be envisaged as being composed of a "true" fatigue mechanism which is represented by fully reversed shear loading ($R = -1$) and a time-at-load mechanism. This statement may be expressed mathematically in terms of crack velocities as

$$\left(\frac{da}{dt}\right)_{total} = \left(\frac{da}{dt}\right)_{fatigue} + \left(\frac{da}{dt}\right)_{time\,at\,load} \tag{5.10}$$

The crack velocity due to true fatigue may be expressed as

$$\left(\frac{da}{dt}\right)_{fatigue} = \frac{dN}{dt}\frac{da}{dN} = f\frac{da}{dN} \tag{5.11}$$

where f is the cyclic frequency. Since crack growth rate, da/dN has been shown to be related to ΔG_{II}, then

$$\left(\frac{da}{dt}\right)_{fatigue} = fA_{-1}(\Delta G_{II})^{n_{-1}} \tag{5.12}$$

where A_{-1} and n_{-1} are experimentally determined fatigue parameters for the $R = -1$ loading case. Based on the observed dependence of crack velocity on G_{II} [39] and due to the fact that time-at-load effects must be related to the average value of G_{II} in a cycle, then

$$\left(\frac{da}{dt}\right)_{time\,at\,load} = B(G_{IImean})^{m} \tag{5.13}$$

where B and m are experimentally determined crack velocity parameters. Since

$$\left(\frac{da}{dN}\right)_{total} = \frac{1}{f}\left(\frac{da}{dt}\right)_{total} \tag{5.14}$$

then substituting equations (5.12) and (5.13) into equation (5.10) and substituting the result into equation (5.14) yields

$$\left(\frac{da}{dN}\right)_{total} = A_{-1}(\Delta G_{II})^{n_{-1}} + \frac{B}{f}(G_{IImean})^{m} \tag{5.15}$$

or, in terms of ΔG_{II}

$$\left(\frac{da}{dN}\right)_{total} = A_{-1}(\Delta G_{II})^{n-1} + \frac{B}{f}\left(\frac{(1+R^2)\Delta G_{II}}{2(1-R^2)}\right)^m \tag{5.16}$$

Compare this equation with the experimentally fitted equation

$$\left(\frac{da}{dN}\right)_{total} = A_{apparent}(\Delta G_{II})^{n_{apparent}} \tag{5.17}$$

where $A_{apparent}$ and $n_{apparent}$ are the same A and n used in equation (4.2), but here the subscripts serve to emphasize the concept that what is considered to be fatigue may in fact be a combination of "true" fatigue plus time-at-load effects.

It is evident from equation (5.16) that as the R-ratio increases the second term becomes larger. This disagrees with the experimental results that show a decrease in the absolute value of the growth rate with increasing R-ratio (when analyzed in terms of G_{II}). However, even though values for B and m are not available for mode II static loading of AS4/3501-6, typically $m > n$ [39]. Thus the effect of increasing R in equation (5.16) is to increase the apparent value of n in Figures 5.2 and 5.3 and equations (4.2) and (5.17), where all growth is attributed to fatigue.

Equation (5.16), as compared to equation (5.17), predicts the correct trend for $n_{G,K}$ as a function of R, but predicts an increase in $A_{G,K}$ as well. Experimentally, it is proposed that a decrease in $A_{G,K}$ leads to either a decrease in growth rate or a slower than expected increase in growth rate. The only mechanism that might lead to lower absolute growth rates would be friction between the crack surfaces, leading to lower crack tip stresses and lower "local" G_{II} and K_{II}. This mechanism has been proposed analytically [47] and is discussed further in the next

section.

5.2.4 Postmortem Fractography

The fracture morphology of a failed component typically provides an indication of the manner in which fracture occurred. The fatigue fracture surfaces of the carbon/epoxy samples cycled at different R-ratios were examined to identify the micromechanism for delamination growth. As a way of introducing the anticipated fracture morphology it is instructive to first consider the differences between typical mode I and mode II fracture surfaces.

It has been shown that the fracture energy for the delamination of brittle matrix composites such as AS4/3501-6 is several times greater in mode II ($500\ J/m^2$) than in mode I ($100\ J/m^2$) [48]. In addition, the resistance to fracture increases as the delamination extends under predominently mode I loading, but remains constant when mode II dominates [48]. Increasing resistance to delamination is caused by a phenomenon known as fibre bridging which occurs when the delamination propagates around a fibre, leaving it to bridge the gap between the crack faces [6]. As the delamination grows, the gap widens and the bridged fibre becomes strained. Some of the strain energy available for crack growth is thereby diverted away from the crack tip by the bridged fibre. During mode II fracture, shear loading results in crack propagation on one side of the matrix layer leading to failure close to the fibre-matrix interface [6]. Ultimately, in both modes of fracture, the fibres are directly involved in the failure mechanism. Thus, delamination does not simply involve the tensile or shear failure of a constrained layer of matrix. The distribution of both fibre and matrix in the interlaminar zone is an important consideration in the analysis of the fracture morphology.

Figures 5.11 and 5.12 are scanning electron microscope (SEM) micrographs of typical mode I and mode II AS4/3501-6 fracture surfaces respectively. Above each micrograph is a

schematic of the effect of the loading geometry on the interlaminar zone. The mode I fracture surface shown in Figure 5.11 is composed of bare fibres and fibre shear-out grooves with a very small degree of matrix deformation as expected due to the brittle nature of this system. The failure mechanism in this instance is interfacial debonding, which is a low energy absorbing mechanism.

The mode II fracture surface shown in Figure 5.12 consists of a form of fibre-matrix interface failure characterized by extensive matrix microcracking. The presence of these matrix microcracks, or hackles, provides a much more tortuous path for the delamination which results in a higher fracture toughness for mode II loading over mode I loading. The hackle formation process is shown schematically above the micrograph in Figure 5.12. The shear stress at the crack tip may be resolved into tension-compression components at 45° to the plane of the plies resulting in the formation of matrix microcracks. The delamination extends by the coalescence of these microcracks which leads to the formation of hackles. Notice that some of the hackles, particularly in the central region of the micrograph (Figure 5.12), are tilted at an angle relative to the plane of the delamination. Mode II behavior therefore, is controlled both by the work required to shear the fibres from the matrix as well as the ease with which tensile failure of the matrix between the fibres can occur.

SEM micrographs of the mode II fatigue fracture surfaces for different R-ratios at similar crack growth rates, da/dN, are presented in Figures 5.13 - 5.18. Each micrograph shows the typical morphology observed for that particular R-ratio. The typicality of the micrographs shown here was confirmed by comparing regions of several fractured specimens which had been subjected to the same R-ratio.

The negative shear ($R < 0$) micrographs (Figures 5.13 and 5.14) do not exhibit the hackle pattern characteristic of mode II failure (compare with Figure 5.12). Instead, the fracture surfaces

feature loose, rounded particles of matrix material. It is possible these loose particles are actually hackles which were torn away and ground up by the mode II sliding motion. In addition, the delamination seems to have propagated through the matrix in the interlaminar zone, as there is little evidence of the presence of fibres or fibre shear-out grooves on the fracture surfaces. Since the shear direction reverses in each cycle during negative shear loading, there would be no preference for the delamination to move toward either side of the interlaminar zone. Thus, it is reasonable that the crack propagates through the matrix only. Similar results were obtained in Ref. [6].

At low positive shear values ($R = 0$ and $R = 0.25$), the fracture surface contains an extensive amount of hackles (see Figures 5.15 and 5.16). In this instance, the hackles are intact and are simply torn from the interlaminar region and strewn across the fracture surface. Evidence of hackle formation decreases as the R-ratio increases (compare Figures 5.15 - 5.18). This is perhaps due to the fact that as the R-ratio increases, the contact force between the crack faces increases, thereby inhibiting hackle formation. Additionally, there is increasing evidence of fibre and fibre shear-out grooves present as the R-ratio increases, indicating that there is a tendency for failure to occur at the fibre-matrix interface as the R-ratio increases. This mechanism is similar to the low energy absorbing mode I mechanism. Hence, it seems that a brittle-like fracture mechanism operates at higher R-ratios. Figure 5.19 shows the fracture surface appearance of a mode I failure at the same magnification as Figures 5.13 - 5.18. Note the similarity between this micrograph and Figure 5.18 which shows the mode II morphology at $R = 0.50$.

If an energy based criterion is the limiting requirement for crack extension to occur, i.e. for new crack surfaces to be created, then the postmortem fracture features should agree with the energy approach presented in Figure 5.2. Figure 5.2 shows that as R-ratio increases at a constant level of ΔG_{II}, the crack growth rate decreases. This implies that more energy is required

to extend a delamination at higher R-ratios. However, at $R = 0.50$, no evidence of a higher energy absorbing mechanism is observed. In fact, the surface features tend to suggest the existence of a low energy brittle failure mechanism, which supports the stress intensity approach of Figure 5.4. With this approach a higher growth rate at high R-ratios is consistent with the more brittle appearance of the fracture surface. At low positive R-ratios such as at $R = 0$, the growth rate is low, and consistent with the more energy-absorbing matrix microcracking or hackling seen on the fracture surface. The resin failure dominated negative shear growth rates lie between the low and high positive shear growth rates.

Both energy and stress requirements must be satisfied before delamination extension can occur. In fact, energy and stress are related by equation (5.2); however, the results presented here suggest that energy is always available in sufficient quantity and that crack growth depends on the stress state ahead of the crack tip, i.e. stress is the limiting factor.

One mechanism that serves as a reasonable explanation for the observed growth rate behaviour is friction. As R-ratio increases, increased friction between the crack faces due to an increase in surface contact forces, absorbs energy and effectively lowers the "local" G_{II} and K_{II}at the crack tip. This causes the growth rate to decrease with increasing R-ratio for the ΔG_{II} case and correspondingly causes the growth rate to increase slower than it should with increasing R-ratio for the ΔK_{II} case. As discussed previously, the fatigue parameter, $A_{G,K}$ is largely responsible for the contradictory growth rate trends observed in Figures 5.2 and 5.4. Equation (5.10) predicts an increase in $A_{G,K}$ with R-ratio whereas experimentally, $A_{G,K}$ decreases with increasing R-ratio. In addition, Figure 5.6 indicates that the effect is more significant when the data is analyzed in terms of G_{II} rather than K_{II}. The effect of friction is therefore neatly reflected in the behaviour of $A_{G,K}$ at high R-ratios. Figure 5.18 shows that at $R = 0.50$, any existing matrix damage remains in place due to the higher surface contact forces.

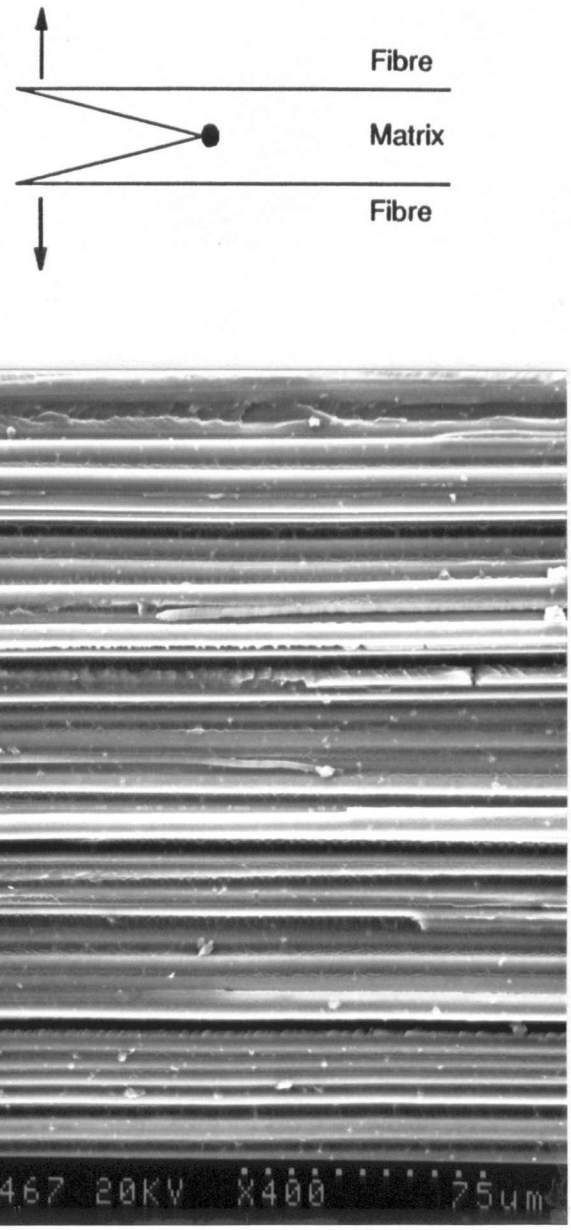

Figure 5.11 SEM micrograph of typical static mode I AS4/3501-6 fracture surface. Note the effect of loading geometry on the interlaminar zone [37].

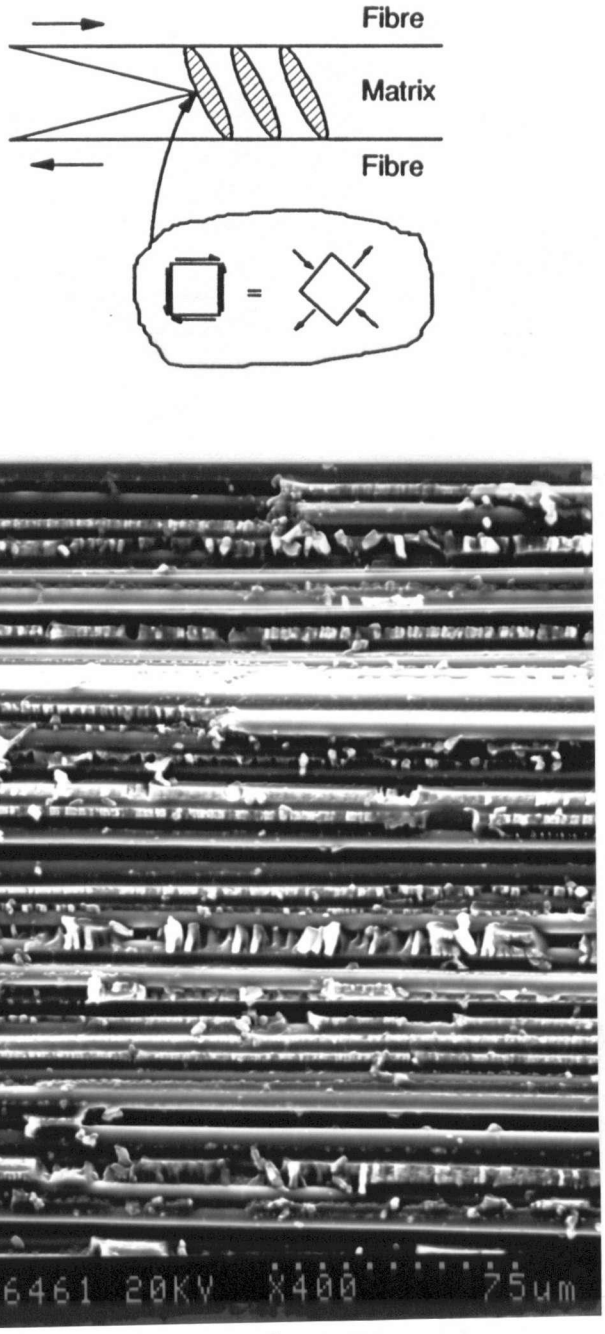

Figure 5.12 SEM micrograph of typical static mode II AS4/3501-6 fracture surface ($R = 0$). Note the effect of loading geometry on the interlaminar zone [37].

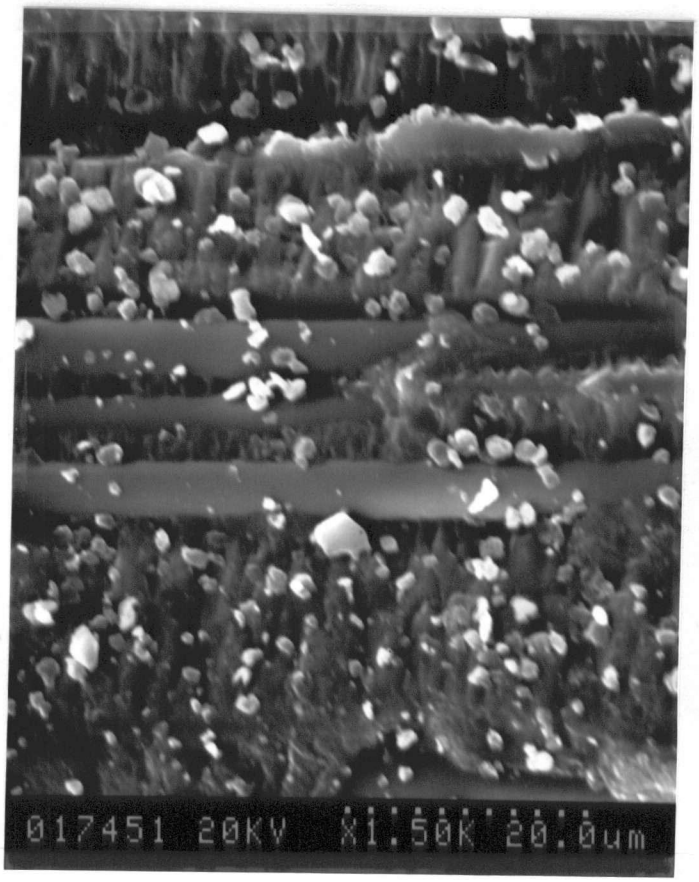

Figure 5.13 SEM micrograph of mode II AS4/3501-6 fatigue fracture surface for R = -1 ($da/dN = 3.49 \times 10^{-4}$ mm/Cycle).

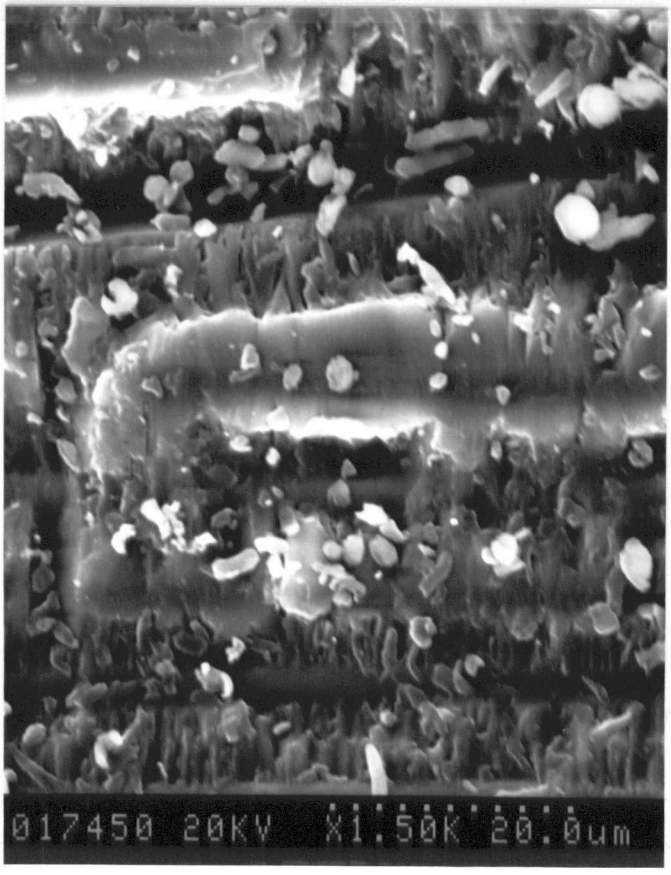

Figure 5.14 SEM micrograph of mode II AS4/3501-6 fatigue fracture surface for R = -0.50 ($da/dN = 1.34 \times 10^{-4}$ mm/Cycle).

Figure 5.15 SEM micrograph of mode II AS4/3501-6 fatigue fracture surface for R = 0 ($da/dN = 3.79 \times 10^{-4}$ mm/Cycle).

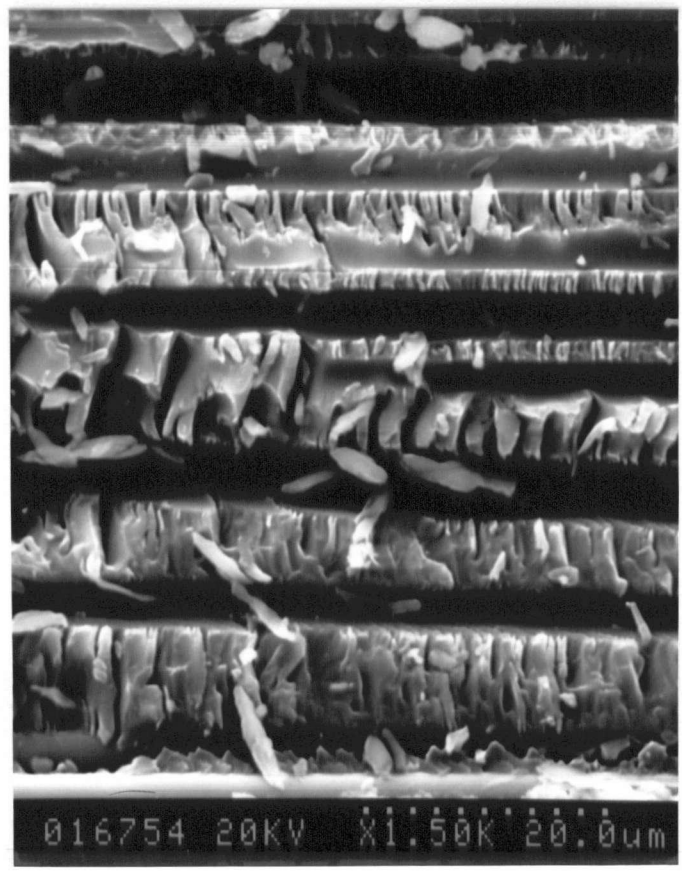

Figure 5.16 SEM micrograph of mode II AS4/3501-6 fatigue fracture surface for R = 0.25 ($da/dN = 6.54 \times 10^{-5}$ mm/Cycle).

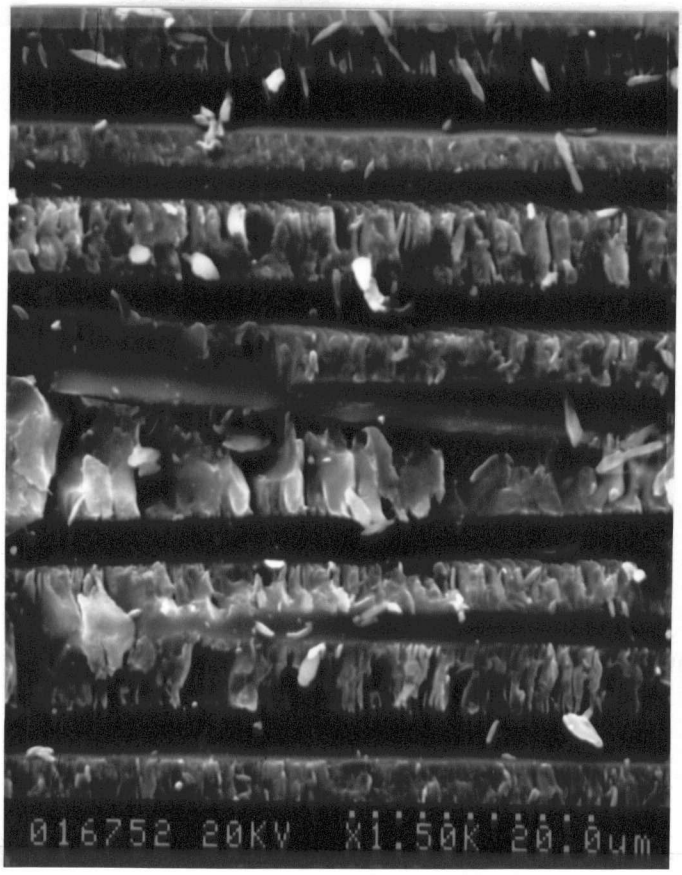

Figure 5.17 SEM micrograph of mode II AS4/3501-6 fatigue fracture surface for R = 0.33 ($da/dN = 1.47 \times 10^{-5}$ mm/Cycle).

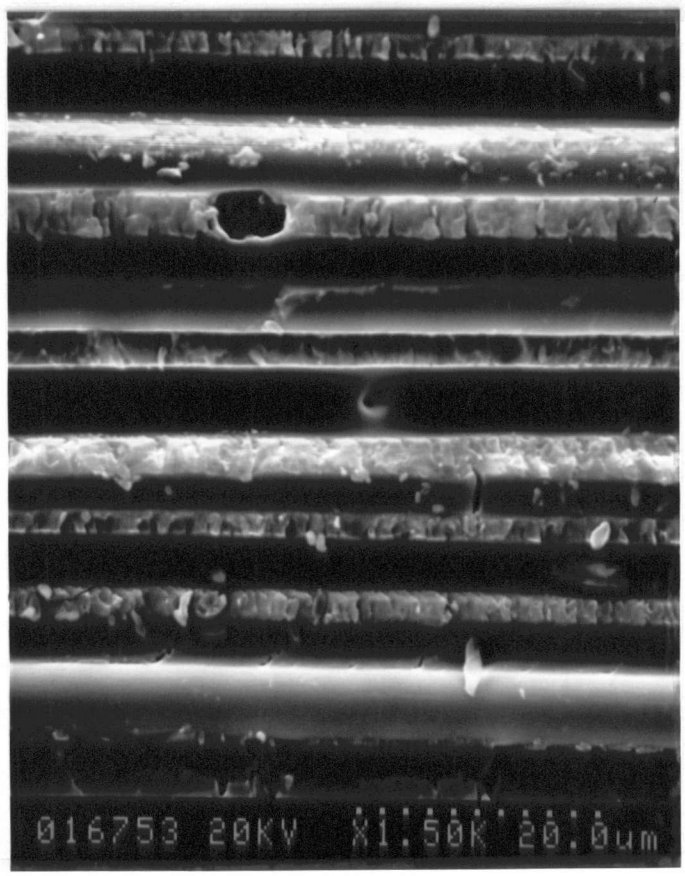

Figure 5.18 SEM micrograph of mode II AS4/3501-6 fatigue fracture surface for R = 0.50 ($da/dN = 4.94 \times 10^{-4}$ mm/Cycle).

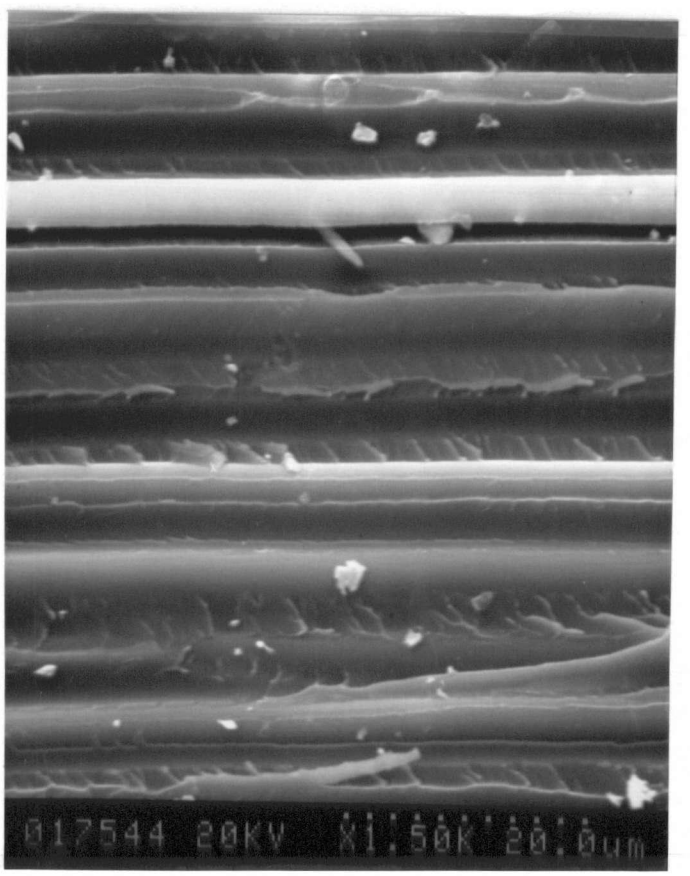

Figure 5.19 SEM micrograph of mode I AS4/3501-6 fracture surface. The magnification is identical to Figures 5.13 - 5.18.

6 CONCLUSIONS

The results of this study on the effect of R-ratio on the fatigue delamination of unidirectional carbon/epoxy composites support the following conclusions:

(1) The crack growth rate, da/dN is dependent upon R-ratio over the range of ΔG_{II} tested.

For a constant level of ΔG_{II}, the crack growth rate decreases as the R-ratio is increased from $R = -1.0$ to $R = 0.50$. A similar trend is observed when the growth rate data is plotted as a function of G_{IImax}.

(2) An asymptote representing a reasonable estimate ($500\ J/m^2$) for the critical value of strain energy release rate, G_{IIc} for the AS4/3501-6 composite system is obtained by extending the growth rate curves (as a function of G_{IImax}) at different R-ratios to a common intersection point.

(3) The effect of plotting da/dN as a function of ΔK_{II} is to produce an R-ratio dependence opposite to that seen by either the ΔG_{II} or G_{IImax} approach. For a constant level of ΔK_{II}, the crack growth rate increases as the R-ratio is increased from $R = 0$ to $R = 0.50$.

(4) The fatigue growth rate exponent, n is large and increases with increasing R-ratio when the growth rate data is analyzed with respect to both ΔG_{II} and ΔK_{II}. Values for n_G range from 3.21 to 20.5 and from 6.42 to 41.0 for n_K.

(5) The fatigue growth rate constant, A decreases with increasing R-ratio when the growth rate data is analyzed with respect to both ΔG_{II} and ΔK_{II}. Values for A_G range from 1.08×10^{-10} to 2.95×10^{-53} and from 1.40×10^{-6} to 2.65×10^{-17} for A_K. The constant A_G is much more sensitive to changes in R-ratio than A_K.

(6) Since the fatigue parameters $n_{G,K}$ and $A_{G,K}$ are uniquely related to R-ratio, master equations which completely characterize the observed fatigue behaviour as a function of ΔG_{II} and ΔK_{II} are proposed for this material system:

$$\frac{da}{dN} = 10^{-20.7(1-R)^{-1.24}} (\Delta G_{II})^{7.53(1-R)^{-1.37}} \tag{6.1}$$

$$\frac{da}{dN} = 10^{-9.72(1-R)^{-0.802}} (\Delta K_{II})^{15.0(1-R)^{-1.37}} \tag{6.2}$$

(7) The characteristic equations provide an excellent fit to the data with deviations occurring as a result of the sensitivity of $A_{G,K}$ to changes or errors in the experimental determination of R-ratio.

(8) Time-at-load considerations establish the correct increasing trend for n as a function of R-ratio, but predict a corresponding increase in A. Friction between the crack faces is proposed as a mechanism which physically lowers the absolute growth rates by affecting A at high R-ratios.

(9) The negative shear ($R < 0$) fracture surface morphology does not feature a characteristic mode II hackle pattern, but rather, loose rounded particles of matrix material. In regions subjected to low positive shear values ($R \approx 0$), the fracture surface contains extensive hackling. Evidence of hackle tearing decreases as the R-ratio is increased to $R = 0.50$, where the fracture surface resembles a mode I fracture surface.

(10) The delamination propagates through the matrix only for the case of negative shear loading. In this instance, the shear direction reverses in each cycle and there is no

preference for the crack to grow toward either side of the interlaminar zone. As the R-ratio is increased to $R = 0.50$, there is an increasing tendency for failure to occur at the fibre/matrix interface.

(11) In general, the fracture surface morphology supports the hypothesis that energy for delamination is always available in sufficient quantity and that growth depends on the stresses ahead of the crack tip being sufficiently high.

7 RECOMMENDATIONS

Regarding future work, the following recommendations are proposed:

(1) Researchers have shown that increasing the matrix toughness of a composite system reduces the slope, n for both $R = -1.0$ and $R = 0$ [25]. As a result, it would be interesting to monitor the corresponding effect of R-ratio on tougher systems such as AS4/PEEK.

(2) Other work has shown that increasing R-ratio from $R = 0.10$ to $R = 0.50$ increases the no-delamination growth threshold value of mode II strain energy release rate, G_{IIth} by *43%* for a toughened composite system [29]. An examination of the effect of R-ratio on G_{IIth} for the current brittle AS4/3501-6 system would provide useful information for the infinite life design approach.

(3) The time-at-load model proposed in equation (5.16) should be tested by obtaining values for B and m for the AS4/3501-6 system. This work should be tied in with an examination of the effect of frequency on growth rate.

(4) The possibility that high contact forces and/or friction may be lowering the "local" G_{II} and K_{II} at the crack tip, resulting in lower absolute growth rates, should be examined further.

REFERENCES

[1] Marshall, J., "Applying Composite Materials to Structures", *Advanced Materials Technology International 1990*, Greville B. Brook, ed., pp 288-290.

[2] Parker, I., "Airbus Stays Ahead", *Aerospace Composites and Materials*, Vol. 1, No. 4, Summer 1989, pp 44-47.

[3] Fong, J.T., "Fatigue Mechanisms", ASTM STP 675, J.T. Fong, ed., American Society for Testing and Materials, Philadelphia, 1979, p. 730.

[4] Tasnon, M., and Roy, C., "Damage Tolerance in Graphite-Epoxy Composite: Comprehensive Monitoring Method", *Polymer Composites*, Vol.8, October 1987, pp 352-

[5] *Delamination and Debonding of Materials*, ASTM STP 876, W.S.Johnson, Ed., American Society for Testing and Materials, Philadelphia, 1985.

[6] Russell, A.J., "Micromechanics of Interlaminar Fracture and Fatigue", *Polymer Composites*, Vol.8, October 1987, pp 342-351.

[7] Vanderkley, P.S., " Mode I - Mode II Delamination Fracture Toughness of a Unidirectional Graphite/Epoxy Composite", Master's Thesis, Texas A&M University, College Station, TX, December 1981.

[8] Martin, R., "Characterizing Delamination Failure of Composite Materials", Seminar presented at U.B.C., October 4, 1988.

[9] Broek, D., *Elementary Engineering Fracture Mechanics*, Fourth Edition, Martinus Nijhoff Publishers, 1986.

[10] Hertzberg, R.W., *Deformation and Fracture Mechanics of Engineering Materials*, John Wiley and Sons, 1976.

[11] Tada,H, Paris ,P.C., and Irwin, G.R., *Stress Analysis of Cracks Handbook*, DEL Research Corp., 1973.

[12] Wu, E.M., "Fracture Mechanics of Anisotropic Plates", *Progress in Material Sciences*, Vol.1, Technomics, Stanford, Connecticut, 1980.

[13] Beaumont, P.W.R., and Tetelman, "The Fracture Strength and Toughness of Fibrous Composites ", *Failure Modes in Composites*, The Metallurgical Society, AIME, 1974, pp 49-80.

[14] Slepetz, J.M., and Carlson, L.A., "Fracture of Compact Tension Specimens", *Fracture Mechanics of Composites*, ASTM STP 593, 1975, pp 143-162.

[15] Wang, S.S., "Fracture Mechanics for Delamination Problems in Composite Materials", Journal of Composite Materials, Vol. 17, May 1983, pp 210-223.

[16] Griffith,A.A., "The Phenomenon of Rupture and Flow in Solids", *Phil. Trans. Royal Society of London*, A221, 1921, pp 163-197.

[17] Jones, R.M., *Mechanics of Composite Materials*, McGraw Hill, New York, 1975, pp 76-80.

[18] Tsai, S.W., "Strength Theories of Filamentary Structures", *Fundamental Aspects of Fibre Reinforced Plastic Composites*, R.T. Schwartz and H.S. Schwartz, eds., Interscience, New York, 1968, Chapter 1.

[19] Hill, R., *The Mathematical Theory of Plasticity*, Oxford University Press, Oxford, 1950.

[20] Reifsneider, K.L., "Life Prediction Analysis: Directions and Divigations", Sixth International Conference on Composite Materials, July 20-24, 1987, pp 4.1-4.31.

[21] Paris, P.C., "The Growth of Fatigue Cracks Due to Variations in Load", Ph.D. Thesis, Lehigh University, 1962.

[22] Wilkins, D.J., Eisenmann, J.R., Camin, R.A., Margolis, W.S. and Benson, R.A., "Characterizing Delamination Growth in Graphite-Epoxy", *Damage in Composite Materials*, ASTM STP 775, K.L. Reifsneider, ed., American Society for Testing and Materials, Philadelphia, 1982, pp 168-183.

[23] Ramkumar, R.L., and Whitcomb, J.D. "Characterization of Mode I and Mixed Mode Delamination Growth in T300/5208 Graphite/Epoxy", *Delamination and Debonding of Materials*, ASTM STP 876, W.S. Johnson, ed., American Society for Testing and Materials, Philadelphia, 1985, pp 315-335.

[24] Bathias, C. and Laksimi, A., "Delamination Threshold and Loading Effect in Fiber Glass Epoxy Composite", *Delamination and Debonding of Materials*, ASTM STP 876, W.S. Johnson, ed., American Society for Testing and Materials, Philadelphia, 1985, pp 217-237.

[25] Russell, A.J. and Street, K.N., "The Effect of Matrix Toughness on Delamination: Static and Fatigue Fracture Under Mode II Shear Loading of Graphite Fibre Composites", *Toughened Composites*, ASTM STP 937, N.J. Johnston, ed., American Society for Testing and Materials, Philadelphia, 1987, pp 275-294.

[26] Tretheway, B.R., Gillespie, J.W. and Carlsson, L.A., "Mode II Cyclic Delamination Growth", *Journal of Composite Materials*, Vol. 22, May 1988, pp 459-483.

[27] Gustafson, C.G. and Hojo, M., "Mode I Delamination Fatigue Growth of Unidirectional Graphite Fiber/PEEK Composites", *Initiation and Growth of Fatigue Damage in Graphite/Epoxy and Graphite/PEEK Laminates*, Report No. 88-9, The Royal Institute of Stockholm, Sweden, 1988.

[28] Hojo, M., Tanaka, K., Gustafson, C.G. and Hayashi, R., "Effect of Stress Ratio on Near Threshold Propagation of Delamination Fatigue Cracks in Unidirectional CFRP", *Composite Science and Technology*, Vol. 29, 1987, pp 273-292.

[29] Martin, R.H. and Murri, G.B., "Characterization of Mode I and Mode II Delamination Growth and Thresholds in AS4/PEEK Composites", Presented at the Ninth ASTM Symposium on Composite Materials: Testing and Design, Reno, Nevada, April 27-29, 1988.

[30] Mall, S., Ramamurthy, G. and Rezaizdeh, A., "Stress Ratio Effect on Cyclic Debonding in Adhesively Bonded Composite Joints", *Composite Structures*, Vol. 8, 1987, pp 31-45.

[31] Donaldson, S.L. and Mall, S., "Delamination Growth in Graphite/Epoxy Composites Subjected to Cyclic Mode III Loading", *Journal of Reinforced Plastics and Composites*, Vol. 8, January 1989, pp 91-103.

[32] Forman, R.G., Kearney, V.E. and Engle, R.M., "Numerical Analysis of Crack Propagation in a Cyclic-Loaded Structure", ASME Trans. J. Basic Eng., Vol. 89D, 1967, p 459.

[33] "Near-Threshold Fatigue-Crack Propagation in Steels", R.O. Ritchie: *International Metals Reviews*, Vol. 24, Nos 5 & 6, 1979, pp 205-230.

[34] Cooper, W.D. and Helfrick, A.D., *Electronic Instrumentation and Measurement Technology*, Prentice Hall, 1985, pp 348-362.

[35] Hercules Product Data Sheet, Wilmington, Delaware, U.S.A., No. 847-4.

[36] Carlsson, L.A., Gillespie, J.W. and Tretheway, B.R., "Mode II Interlaminar Fracture of Graphite/Epoxy and Graphite/PEEK", *Journal of Reinforced Plastics and Composites*, Vol. 5, July 1986, pp 170-187.

[37] O'Brien, T.K., Murri, G.B. and Salpekar, S.A., "Interlaminar Shear Fracture Toughness and Fatigue Thresholds for Composite Materials", *Composite Materials: Fatigue and Fracture*, Second Volume, ASTM STP 1012, P.A. Lagace, ed., American Society for Testing and Materials, Philadelphia, 1989, pp 222-250.

[38] Corleto, C.R. and Bradley, W.L., "Mode II Delamination Fracture Toughness of Unidirectional Graphite/Epoxy Composites", *Composite Materials: Fatigue and Fracture*, Second Volume, ASTM STP 1012, P.A. Lagace, ed., American Society for Testing and Materials, Philadelphia, 1989, pp 201-221.

[39] Russell, A.J., "Initiation of Mode II Delamination in Toughened Composites", Presented at the Third ASTM Symposium on Composite Materials: Fatigue and Fracture, Orlando, Florida, November 6-7, 1989.

[40] Prel, Y.J., Davies, P. Benzeggagh, M.L. and de Charentenay, F.X., "Mode II Delamination of Thermosetting and Thermoplastic Composites", Presented at the Second ASTM Symposium on Composite Materials: Fatigue and Fracture, Cincinnati, Ohio, April, 1987.

[41] Poursartip, A. and Chinatambi, N., "An Investigation of Delamination Damage Growth in CFRP Laminates", Presented at the Ninth ASTM Symposium on Composite Materials: Testing and Design, Reno, Nevada, April 27-29, 1988.

[42] Sih, G.C., Paris, P.C. and Irwin, G.R., "On Cracks in Rectilinearly Anisotropic Bodies", *International Journal of Fracture Mechanics*, Vol. 1, 1965, pp 189-202.

[43] Tsai, S.W., *Composites Design*, Fourth Edition, Think Composites Publishers, 1988.

[44] *Damage Tolerant Design Handbook*, Battelle Metals and Ceramic Information Center, Columbus, Ohio, 1975.

[45] Mall, S., Yun, K. and Kochhar, N.K., "Characterization of Matrix Toughness Effect on Cyclic Delamination Growth in Graphite Fiber Composites", *Composite Materials: Fatigue and Fracture*, Second Volume, ASTM STP 1012, P. A. Lagace, ed., American Society for Testing and Materials, Philadelphia, 1989, pp 296-310.

[46] Lee, J.R. and de Charentenay, F.X., "Short Holding Time Effect on Fatigue Behaviour of Unnotched Graphite/Epoxy Laminates", *Journal of Composite Materials*, Vol. 23, September 1989, pp 912-921.

[47] Evans, A.G. and Hutchinson, J.W., "Effects of Non-Planarity on the Mixed Mode Fracture Resistance of Bimaterial Interfaces", *Acta Metallurgica*, Vol. 37, No. 3, 1989, pp 909-916.

[48] Russell, A.J. and Street, K.N., ASTM STP 876, American Society for Testing and Materials, Philadelphia, 1985, pp 349-370.

APPENDIX A

A tabulation of the data generated in this study of unidirectional AS4/3501-6 carbon/epoxy composite specimens is provided in the current section. In the following tables the number of cycles, "N" is presented as a cumulative tally of elapsed cycles to give the quoted crack length measurement. "Optical a" refers to the crack length obtained after "N" cycles as measured with an optical travelling microscope. "Inferred a" is calculated from an expression of the form of equation (3.1) but specific to each specimen. Compliance, "C" is defined as the achieved specimen compliance as determined from the average of the slopes of three successive deflection/load data logging cycles. The mode II strain energy release rate range,"ΔG_{II}" is calculated from equation (4.4). The maximum mode II strain energy release rate, "G_{IImax}" is also calculated from equation (4.4) but with $\delta_{min} = 0$. Finally, the mode II stress intensity factor range, "ΔK_{II}" is calculated from equations (5.1) and (5.2).

Specimen: F11
R-Ratio: 0
δ_{max}: 11 mm

Length, L: 110 mm
Width, b: 20.02 mm
Thickness, 2h: 3.31 mm

N (Cycles)	Optical a (mm)	Inferred a (mm)	C ($\times 10^{-5}$m/N)	ΔG_{II} (J/m^2)
5	25.60	30.00	8.07	159.27
4007	27.53	30.35	8.08	162.38
8009	27.53	30.29	8.08	161.91
12011	28.15	26.47	7.95	127.69
16013	28.15	29.87	8.07	158.05
20015	28.15	29.27	8.04	152.58
24014	28.15	30.35	8.08	162.38
26019	28.15	30.29	8.08	161.91
28021	28.15	28.29	8.01	143.74
30026	28.82	29.68	8.06	156.33
32025	29.48	34.56	8.27	201.25
34027	30.36	33.16	8.20	188.36
36029	31.24	31.13	8.12	169.58
38031	31.88	33.53	8.22	191.73
40033	32.52	35.70	8.33	211.73
42035	33.58	36.29	8.36	217.12
44037	34.30	31.97	8.15	177.32
46039	34.49	34.64	8.27	201.98
48041	34.87	34.20	8.25	197.89
50043	35.17	39.41	8.55	244.94
52045	36.44	41.25	8.67	260.62
54547	40.10	44.64	8.94	287.62
55550	42.30	46.91	9.13	303.92
56552	47.14	49.02	9.34	317.58
57554	51.17	52.82	9.75	338.21
58556	59.33	59.35	10.6	360.53
59058	65.77	65.64	11.6	366.48
59560	73.30	75.00	13.6	351.51
60062	82.76	83.62	15.9	320.71
60564	88.59	89.00	17.5	297.06

Specimen: F12
R-Ratio: 0
δ_{max}: 11 mm

Length, L: 110 mm
Width, b: 19.92 mm
Thickness, 2h: 3.40 mm

N (Cycles)	Optical a (mm)	Inferred a (mm)	C ($\times 10^{-5}$m/N)	ΔG_{II} (J/m^2)
5	28.38	28.99	7.18	166.93
4007	28.38	30.25	7.22	179.74
8009	28.38	31.14	7.25	188.84
12011	28.71	29.95	7.21	176.70
16013	29.29	31.17	7.25	189.13
20015	31.04	31.71	7.27	194.75
24017	32.10	33.03	7.32	208.31
28019	35.27	34.77	7.40	226.25
30021	36.60	36.40	7.47	242.84
32023	38.19	38.72	7.59	266.09
34025	40.39	41.60	7.76	293.74
35027	41.50	43.51	7.89	311.01
36029	43.96	46.59	8.12	336.56
37031	50.12	52.85	8.70	377.91
37533	60.23	63.62	10.1	409.99
38034	91.59	93.50	17.0	311.32

Specimen: F16
R-Ratio: 0, 0.25, 0.50
δ_{max}: 6 mm, 8 mm, 12 mm

Length, L: 110 mm
Width, b: 19.98 mm
Thickness, 2h: 3.35 mm

N (Cycles)	R-Ratio	Inferred a (mm)	C ($\times 10^{-5}$m/N)	ΔG_{II} (J/m^2)	G_{IImax} (J/m^2)	ΔK_{II} ($MPa\sqrt{m}$)
3	0	28.43	7.40	-	-	-
11515	0	40.45	7.95	-	-	-
204527	0	42.04	8.05	88.78	88.78	2.18
206530	0.50	43.03	8.12	280.37	373.82	2.23
351539	0	42.63	8.09	96.28	96.28	2.27
351842	0.50	44.27	8.21	285.44	380.58	2.25
461851	0	45.71	8.32	99.69	99.69	2.31
461884	0.50	46.74	8.40	310.33	413.78	2.35
533890	0	48.28	8.54	106.02	106.02	2.38
533894	0.50	49.73	8.67	328.79	438.39	2.42
583900	0	52.86	8.98	112.81	112.81	2.45
584403	0.25	53.36	9.03	197.87	211.06	2.52
622409	0	55.46	9.27	119.54	119.54	2.53
622665	0.25	56.03	9.34	204.39	218.02	2.56
647668	0	57.78	9.55	123.37	123.37	2.51
647823	0.25	58.51	9.65	208.96	222.89	2.59
670029	0	59.74	9.81	126.04	126.04	2.60
670163	0.25	60.68	9.94	211.74	225.86	2.60
695169	0	62.34	10.2	127.69	127.69	2.61
695263	0.25	63.15	10.3	214.17	228.45	2.62
714269	0	64.88	10.6	128.79	128.79	2.62
714373	0.25	65.31	10.6	215.16	229.50	2.63
728376	0	66.94	10.9	129.11	129.11	2.63
728490	0.25	67.58	11.0	214.98	229.31	2.63
744096	0	68.65	11.2	128.84	128.84	2.62
744500	0.25	70.02	11.5	214.18	228.46	2.62
759505	0	71.08	11.7	127.91	127.91	2.61
759659	0.25	72.10	11.9	212.18	226.36	2.61
783665	0	74.36	12.3	126.64	126.64	2.60
783769	0.25	74.59	12.4	208.03	221.90	2.58
799772	0	75.89	12.6	124.60	124.60	2.58
799926	0.25	76.80	12.9	205.56	219.26	2.57
819929	0	78.15	13.2	122.38	122.38	2.56
820133	0.25	78.75	13.3	201.41	214.84	2.54
840136	0	79.96	13.6	120.14	120.14	2.53
840440	0.25	80.41	13.7	197.71	210.89	2.52
870443	0	82.59	14.2	118.05	118.05	2.51
870847	0.25	82.94	14.3	191.83	204.62	2.48
905850	0	84.51	14.8	114.61	114.61	2.48
906855	0.25	85.20	15.0	187.22	199.70	2.45
946858	0	85.85	15.1	111.30	111.13	2.44
947862	0.25	87.15	15.5	183.87	196.13	2.43
997865	0	87.70	15.7	108.33	108.33	2.41

Specimen: F17
R-Ratio: 0.25, 0.33, 0.50
δ_{max}: 8 mm, 9 mm, 12 mm

Length, L: 110 mm
Width, b: 20.13 mm
Thickness, 2h: 3.22 mm

N (Cycles)	R-Ratio	Inferred a (mm)	C ($\times 10^{-5}$m/N)	ΔG_{II} (J/m^2)	G_{IImax} (J/m^2)	ΔK_{II} ($MPa\sqrt{m}$)
3	0	28.94	8.07	-	-	-
27012	0	34.92	8.33	-	-	-
230015	0.25	37.00	8.44	110.62	118.00	2.54
378018	0.33	38.07	8.51	145.06	163.19	1.97
595021	0.25	38.21	8.52	126.07	134.48	2.52
790024	0.33	38.79	8.55	152.09	171.10	2.02
985027	0.25	37.31	8.46	129.52	138.15	2.48
1180030	0.33	38.25	8.52	169.45	190.63	2.13
1376033	0.25	41.82	8.76	126.94	134.4	2.45
1390036	0.50	38.68	8.55	232.19	309.59	2.03
1520039	0.33	41.31	8.72	195.56	220.01	2.29
1524042	0.50	43.99	8.93	275.10	366.80	2.21

Specimen: F18
R-Ratio: 0.14, 0.25, 0.33, 0.50
δ_{max}: 7 mm, 8 mm, 9 mm, 12 mm

Length, L: 110 mm
Width, b: 20.17 mm
Thickness, 2h: 3.31 mm

N (Cycles)	R-Ratio	Inferred a (mm)	C ($\times 10^{-5}$m/N)	ΔG_{II} (J/m^2)	G_{IImax} (J/m^2)	ΔK_{II} ($MPa\sqrt{m}$)
3	0	37.05	7.76	-	-	-
10007	0	38.52	7.84	-	-	-
110013	0.33	40.89	7.99	158.85	178.70	2.06
113016	0.50	41.13	8.00	252.19	336.26	2.12
213019	0.33	41.66	8.04	182.60	205.42	2.21
213522	0.50	42.20	8.07	276.02	368.03	2.22
270525	0.33	43.72	8.18	187.13	210.53	2.23
271628	0.50	45.63	8.33	285.39	380.52	2.25
302631	0.33	46.31	8.39	198.77	223.62	2.30
302834	0.50	47.83	8.52	313.28	417.71	2.36
312837	0.33	50.12	8.74	212.26	238.79	2.38
347840	0.25	51.31	8.85	182.92	195.11	2.42
381843	0.14	53.27	9.06	152.88	156.07	2.48
391846	0.25	53.94	9.14	204.42	218.05	2.56
409849	0.14	54.85	9.24	160.41	163.76	2.54
410052	0.33	55.95	9.38	242.68	273.01	2.55
423055	0.14	56.02	9.39	163.51	166.91	2.56
424058	0.25	56.70	9.47	206.72	220.51	2.57
432061	0.14	57.78	9.61	165.48	168.93	2.57
435064	0.25	58.60	9.72	208.16	222.03	2.58
443067	0.14	58.94	9.76	167.98	171.48	2.59
446070	0.14	59.61	9.85	168.95	172.47	2.60
448273	0.14	60.06	9.92	169.33	172.86	2.60
463976	0.14	62.86	10.3	169.99	173.53	2.61
493979	0.14	64.26	10.5	170.36	173.91	2.61
513982	0.14	67.22	11.0	172.00	175.58	2.63
543985	0.14	69.84	11.5	172.31	175.90	2.63
573988	0.14	73.00	12.1	171.88	175.46	2.62

Specimen: F19
R-Ratio: 0.25, 0.40
δ_{max}: 8 mm, 10 mm

Length, L: 110 mm
Width, b: 20.21 mm
Thickness, 2h: 3.35 mm

N (Cycles)	R-Ratio	Inferred a (mm)	C ($\times 10^{-5}$m/N)	ΔG_{II} (J/m^2)	G_{IImax} (J/m^2)	ΔK_{II} ($MPa\sqrt{m}$)
3	0	29.99	7.36	-	-	-
9010	0	39.54	7.83	-	-	-
64013	0.40	42.87	8.07	239.89	285.59	2.34
76016	0.40	43.90	8.15	246.67	293.66	2.38
81019	0.40	45.46	8.27	256.42	305.26	2.42
84522	0.40	47.10	8.42	265.98	316.64	2.47
105344	0.25	47.74	8.48	204.42	218.05	2.56
105847	0.40	48.04	8.50	271.07	322.71	2.49
120850	0.25	50.66	8.76	206.72	220.51	2.57
121153	0.40	50.69	8.77	286.49	341.07	2.56
121756	0.40	51.30	8.83	292.62	348.36	2.59
129759	0.25	52.25	8.94	208.16	222.03	2.58
129912	0.40	52.86	9.00	295.92	352.29	2.60
130015	0.40	53.80	9.11	296.50	352.98	2.60

Specimen: F20
R-Ratio: -0.50, -1.00
δ_{max}: 6 mm, 6 mm

Length, L: 110 mm
Width, b: 20.09 mm
Thickness, 2h: 3.36 mm

N (Cycles)	R-Ratio	Inferred a (mm)	C ($\times 10^{-5}$m/N)	ΔG_{II} (J/m^2)	G_{IImax} (J/m^2)	ΔK_{II} ($MPa\sqrt{m}$)
3	0	29.49	7.18	-	-	-
16010	0	35.31	7.41	-	-	-
26013	-1.00	38.81	7.59	86.19	86.19	2.14
32016	-0.50	39.62	7.63	88.77	88.77	2.15
35019	-1.00	40.95	7.71	92.87	92.87	2.23
41022	-0.50	42.30	7.80	96.92	96.92	2.28
43025	-1.00	43.29	7.86	99.81	99.81	2.31
49028	-0.50	44.85	7.98	104.15	104.15	2.36
50531	-1.00	46.14	8.07	107.56	107.56	2.40
53534	-0.50	47.28	8.17	110.44	110.44	2.43
55037	-1.00	49.20	8.33	114.91	114.91	2.48
57040	-0.50	49.84	8.39	116.31	116.31	2.49
58043	-1.00	50.07	8.41	116.80	116.80	2.50
60046	-0.50	52.29	8.62	121.13	121.13	2.54
61049	-1.00	53.21	8.72	122.75	122.75	2.56
63052	-0.50	54.51	8.85	124.82	124.82	2.58
64055	-1.00	55.49	8.96	126.22	126.22	2.60
66058	-0.50	56.33	9.06	127.31	127.31	2.61
67061	-1.00	57.53	9.20	128.70	128.70	2.62
69064	-0.50	58.53	9.33	129.70	129.70	2.63
70067	-1.00	59.85	9.50	130.81	130.81	2.64
72070	-0.50	61.11	9.67	131.63	131.63	2.65
73073	-1.00	62.82	9.91	132.41	132.41	2.66
75076	-0.50	62.80	9.90	132.40	132.40	2.66